Mon. Not. R. Astron. Soc. **000**, 1–21 (2002) Printed 18 March 2011 (MN LATEX style file v2.2)

Dynamical masses of early-type galaxies: a comparison to lensing results and implications for the stellar IMF and the distribution of dark matter

J. Thomas[1,2⋆], R. P. Saglia[1,2], R. Bender[1,2], D. Thomas[3], K. Gebhardt[4], J. Magorrian[5], E. M. Corsini[6], G. Wegner[7] and S. Seitz[1,2]

[1] *Universitätssternwarte München, Scheinerstraße 1, D-81679 München, Germany*
[2] *Max-Planck-Institut für Extraterrestrische Physik, Giessenbachstraße, D-85748 Garching, Germany*
[3] *Institute of Cosmology and Gravitation, University of Portsmouth, Dennis Sciama Building, Burnaby Road, Portsmouth, PO1 3FX, UK*
[4] *Department of Astronomy, University of Texas at Austin, C1400, Austin, TX78712, USA*
[5] *Theoretical Physics, Department of Physics, University of Oxford, 1 Keble Road, Oxford U.K., OX1 3NP*
[6] *Dipartimento di Astronomia, Università di Padova, vicolo dell'Osservatorio 2, I-35122 Padova, Italy*
[7] *Department of Physics and Astronomy, 6127 Wilder Laboratory, Dartmouth College, Hanover, NH 03755-3528, USA*

Accepted 1988 December 15. Received 1988 December 14; in original form 1988 October 11

ABSTRACT

This work aims to study the distribution of luminous and dark matter in Coma early-type galaxies. Dynamical masses obtained under the assumption that mass follows light do not match with the masses of strong gravitational lens systems of similar velocity dispersions. Instead, dynamical fits with dark matter halos are in good agreement with lensing results. We derive mass-to-light ratios of the stellar populations from Lick absorption line indices, reproducing well the observed galaxy colours. Even in dynamical models with dark matter halos the amount of mass that follows the light increases more rapidly with galaxy velocity dispersion than expected for a constant stellar initial mass function (IMF). While galaxies around $\sigma_{\rm eff} \approx 200\,$km/s are consistent with a Kroupa IMF, the same IMF underpredicts luminous dynamical masses of galaxies with $\sigma_{\rm eff} \approx 300\,$km/s by a factor of two and more. A systematic variation of the stellar IMF with galaxy velocity dispersion could explain this trend with a Salpeter IMF for the most massive galaxies. If the IMF is instead constant, then some of the dark matter in high velocity dispersion galaxies must follow a spatial distribution very similar to that of the light. A combination of both, a varying IMF and a component of dark matter that follows the light is possible as well. For a subsample of galaxies with old stellar populations we show that the tilt in the fundamental plane can be explained by systematic variations of the total (stellar + dark) mass inside the effective radius. We tested commonly used mass estimator formulae, finding them accurate at the $20-30\,\%$ level.

Key words: galaxies: elliptical and lenticular, cD – galaxies: kinematics and dynamics — galaxies: structure

1 INTRODUCTION

The masses of galaxies are revealed by the gravitational interaction of their matter constituents, e.g. by stellar or gas kinematics or gravitational lensing effects. The caveat is that these effects rigorously constrain only the total amount of gravitating mass. The decomposition into luminous and dark matter relies on further assumptions. For example, in dynamical studies of early-type galaxies it is commonly assumed that the stellar mass distribution follows the light. Any radial increase in the mass-to-light ratio – if needed to explain the observed velocities of the stars – is attributed to dark matter.

The limitation of this approach becomes clear if one imagines a galaxy dark matter halo that follows the light distribution exactly. Discriminating between luminous and dark matter according to their potentially different radial distributions would fail in this case. In fact, there would be no direct way to dynamically unravel the relative contributions of luminous and dark matter to the galaxy mass. It

⋆ E-mail: jthomas@mpe.mpg.de

is unlikely that a real galaxy halo follows the light distribution exactly, yet it exemplifies the intrinsic degeneracies in any mass decomposition. On top of this, even the most advanced present-day dynamical modelling techniques rely on symmetry assumptions and, often, also on the assumption of a steady-state dynamical system. If the symmetry assumptions are strongly violated, dynamical mass-to-light ratios can be biased by a factor of up to two (Thomas et al. 2007a).

To crosscheck the validity of the assumptions in dynamical modelling it is important to compare the resulting masses with other independent methods. *Total* masses can be most directly compared to results from gravitational lensing, which is the first goal of this paper.

An examination of the mass *decomposition* requires the investigation of a galaxy's stellar population. Since the latter provides an independent measure of the stellar mass-to-light ratio, the comparison of dynamical and stellar-population masses yields further constraints on the dark matter content. In the above mentioned case, for example, the dynamical mass-to-light ratio $\Upsilon_{*,\rm dyn}$ would exceed the corresponding stellar population value, indicating that some fraction of the galaxy's mass is actually dark matter.

Unfortunately, stellar population models do not provide unique stellar mass-to-light ratios. They suffer from an incomplete knowledge of the initial stellar mass function (IMF), as well as age-metallicity degeneracies. Observations in and around our own Galaxy indicate that the IMF slope flattens below $0.5\,\mathrm{M}_\odot$ (Scalo 1986; Kroupa 2001). Recent spectroscopic observations of massive ellipticals in the near-infrared point towards the low-mass slope of the IMF in these galaxies being steeper (van Dokkum & Conroy 2010). Yet, until now the IMF in distant galaxies with unresolved stellar populations remains largely uncertain. This translates into a significant indeterminacy of population mass-to-light ratios: the steeper the slope at the low-mass end, the higher the population mass-to-light ratio. Hence, the stellar population approach is not directly conclusive as a probe of the mass decomposition in dynamical models.

Conversely, if dynamical stellar mass determinations were free of ambiguities with respect to a dark matter contamination then they could serve as a measure for the slope of the IMF in distant galaxies. The method would be to tweak the IMF in the stellar population models until agreement with the dynamical stellar masses is achieved.

The ambiguities in both, dynamical stellar masses as well as stellar population models, make neither of the approaches directly applicable. Nevertheless, comparing dynamical with stellar population models is important to (1) narrow down the dynamically plausible range of possible IMFs and to (2) delimit the range of dark matter fractions compatible with observed stellar population properties. This is the second goal of the present paper in which we compare dynamical and stellar population masses in a sample of 16 Coma early-type galaxies.

Our dynamical models account for both the full variety of possible orbit configurations in axisymmetric, flattened galaxies as well as for dark matter. In this respect we extend previous studies. Cappellari et al. (2006), for example, used a similar modelling technique to compare dynamical and stellar population masses in the SAURON sample, but they did not consider dark matter explicitly in their dynamical models. The justification for this neglect was the expected insignificance of dark matter in the central galaxy regions probed by the SAURON observations ($r_{\rm obs,max} \lesssim r_{\rm eff}$). However, measuring only the sum of luminous and dark mass makes the comparison with stellar population models potentially uncertain. Napolitano et al. (2010) analysed a large sample of early-type galaxies taking into account the contribution from dark matter, but their models do not account for galaxy flattening and rotation.

A subsample of the Coma galaxies was recently analysed by Grillo & Gobat (2010). While they used multi-band photometry to derive stellar population properties, our approach is to measure ages, metallicities and [α/Fe] ratios from Lick indices to reduce potential biases in population parameters. Likewise, the analysis of SLACS galaxies by Treu et al. (2010), combining constraints from gravitational lensing and stellar dynamics, relied on multi-band photometry for the stellar population part.

Mass-to-light ratios of early-type galaxies are of particular interest to understand the tilt of the fundamental plane. Virial relations imply that the effective surface brightness $\langle I \rangle_{\rm eff}$, the effective radius $r_{\rm eff}$ and the central velocity dispersion σ_0 in hot stellar systems are not independent of each other. This is revealed by the fundamental plane of early-type galaxies (Djorgovski & Davis 1987; Dressler et al. 1987). Yet, the observed fundamental plane is tilted with respect to the simple case of a virialised, homologous family of dynamical systems. This tilt can reflect (1) systematic variations of the luminosity distribution (e.g. Saglia et al. 1993; Trujillo et al. 2004), (2) systematic variations of the orbital structure (e.g. Ciotti et al. 1996) or (3) systematic variations of the mass-to-light ratio, as a result of varying stellar populations and/or dark matter distributions (e.g. Renzini & Ciotti 1993). Understanding these variations allows a deeper insight into the formation process of early-type galaxies (Bender et al. 1992).

Most of the above mentioned effects can be factored out if additional information about the stellar populations and/or the mass distributions are available. Aperture spectroscopy is one way to measure stellar population properties. By assuming simple scaling laws it can also provide estimates for dynamical masses, such that the contributions of stellar population and dynamical effects on the fundamental plane tilt can be disentangled (e.g. Hyde & Bernardi 2009; Graves & Faber 2010). More reliable constraints come from radially resolved spectroscopy and detailed dynamical (or lensing) models of galaxies (e.g. Cappellari et al. 2006; Bolton et al. 2007). The third goal of this paper is to follow the latter approach and to use the specific information contained in our two-component dynamical models for further investigations upon the origin of the fundamental plane tilt.

The paper is organised as follows. Sec. 2 reviews the galaxy sample and models. in Sec. 3 we compare projected masses from dynamical models and from gravitational lensing against each other. Sec. 4 deals with the comparison of luminous dynamical and stellar population masses. The dark matter distribution is analysed in Sec. 5 and implications for the tilt of the fundamental plane are addressed in Sec. 6. The paper is summarised in Sec. 7.

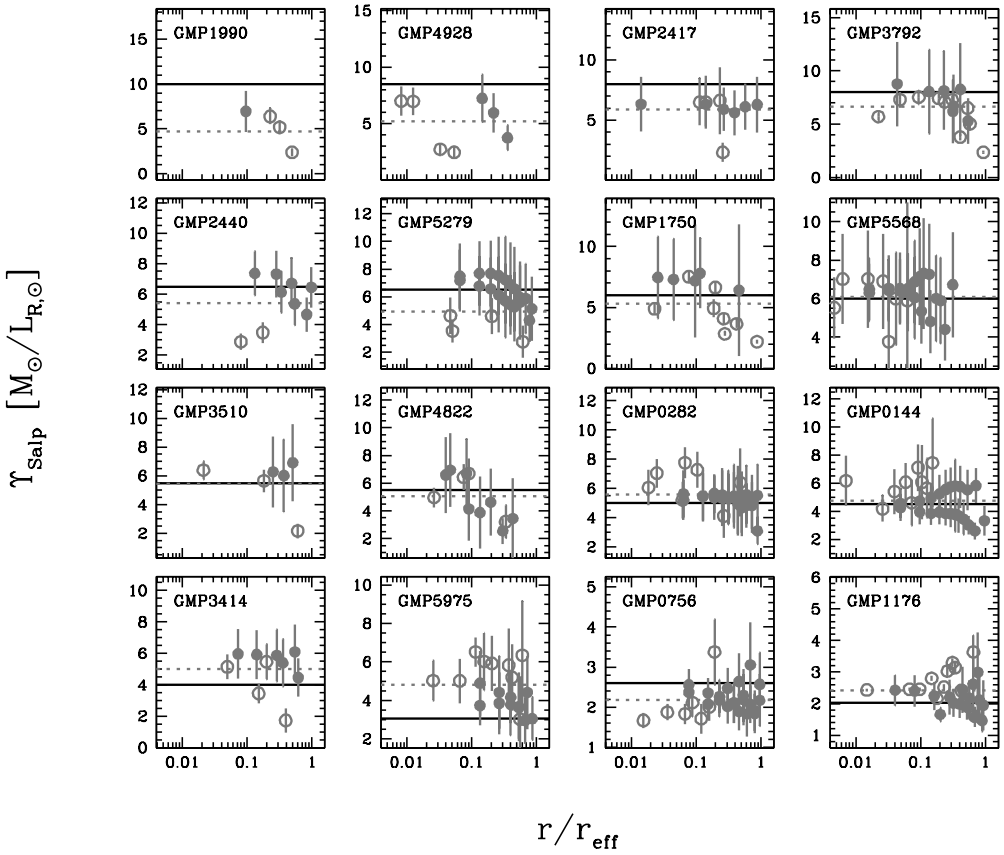

Figure 1. Stellar population mass-to-light ratios $\Upsilon_{\rm Salp}$ (Salpeter IMF) as function of radius along the major-axis (filled circles) and minor-axis (open circles). Note that for some galaxies there are systematic differences between the two sides of a slit which are slightly larger than the statistical errors (e.g. along the major-axis of GMP0144). The dotted line in each panel is the light-weighted average of $\Upsilon_{\rm Salp}$ within $r < r_{\rm eff}$, the solid line corresponds to the stellar mass-to-light ratio $\Upsilon_{*,\rm dyn}$ from dynamical models. From top-left to bottom-right galaxies are plotted in order of decreasing $\Upsilon_{*,\rm dyn}$.

2 GALAXY SAMPLE AND MODELLING

The sample analysed in this paper comprises 16 Coma early-type galaxies in the luminosity range between $M_B = -19.88$ and $M_B = -22.26$ (eight giant ellipticals, eight lenticular/intermediate type galaxies). It is almost identical to the sample presented in Thomas et al. (2009b). Only the galaxy GMP3958 has been omitted for its strong gas emission, which hampers reliable stellar population modelling.

For the dynamical analysis of each galaxy a composite of ground-based and HST photometry has been used. Stellar absorption line data for the kinematics and Lick indices come from various long-slit spectra, at least along the major and minor axes, but in many cases covering other position angles as well. The spectra extend to $1-4\,r_{\rm eff}$. Details about the photometric and spectroscopic data have been published in Mehlert et al. (2000), Wegner et al. (2002), Corsini et al. (2008), and Thomas et al. (2009b).

2.1 Dynamical modelling

To the kinematic and photometric data we applied our implementation of Schwarzschild's orbit superposition technique (Schwarzschild 1979) for axisymmetric potentials (Richstone & Tremaine 1988; Gebhardt et al. 2003; Thomas et al. 2004, 2005a). A detailed description of the models is given in Thomas et al. (2007b). Most important for this paper are the assumptions about the mass structure. We will consider two sets of models. For the first set it is assumed that all the mass follows the light, i.e.

$$\rho = \Upsilon \times \nu \tag{1}$$

where ν is the three-dimensional luminosity density. By construction, the mass-to-light ratio Υ here includes the contribution of both the stellar and dark mass of a galaxy. It is not known in advance and obtained by a χ^2-minimisation with respect to the kinematical observations. The best-fit Υ of one-component (i.e. self consistent) models will be referred to as $\Upsilon_{*,\rm sc}$ in the remainder of this paper and can be found in Tab. 1.

For the second, and standard set of models we assume a mass density of the form

$$\rho = \Upsilon \times \nu + \rho_{\rm DM}. \tag{2}$$

The first component again follows the light, while the second one, $\rho_{\rm DM}$, accounts for dark matter. Eq. 2 is designed to

separate the contributions of luminous and dark matter to the total mass of a galaxy. Our basic assumption is that the best-fit Υ of two-component models represents only the stellar mass of a galaxy and we will refer to it as the dynamical stellar mass-to-light ratio $\Upsilon_{*,\rm dyn}$ in the following. Strictly speaking, $\Upsilon_{*,\rm dyn}$ measures all the mass which follows the light distribution, be it stellar or be it dark matter. In this respect $\Upsilon_{*,\rm dyn}$ provides only an upper limit for the stellar mass. As soon as there are other mass components which – for whatever reason – follow the light, they will contribute to $\Upsilon_{*,\rm dyn}$ as well and the actual galaxy stellar mass-to-light ratio will be smaller than $\Upsilon_{*,\rm dyn}$. A more detailed discussion upon this issue will be given in Secs. 4.4 and 5.2.

According to equation (2), the cumulative (spherical) dark matter fraction $f_{\rm DM,dyn}$ of the models inside radius r is

$$f_{\rm DM,dyn}(r) \equiv \frac{M_{\rm DM,dyn}(r)}{M_{\rm tot,dyn}(r)} = \frac{M_{\rm DM,dyn}(r)}{\Upsilon_{*,\rm dyn}\,L(r) + M_{\rm DM,dyn}(r)}, \quad (3)$$

where $M_{\rm tot,dyn}$, $M_{\rm DM,dyn}$ and L stand for the cumulative total mass, dark mass and light inside radius r. Tab. 1 lists the observationally derived dark matter fractions. Here we consider mostly the region inside $r_{\rm eff}$, where the average dark matter fraction is $\langle f_{\rm DM,dyn}\rangle = 23 \pm 17\,\%$, but our data reach out to radii where the stellar and the dark matter density become equal (Thomas et al. 2007b).

We probed two dark matter descriptions. Firstly, logarithmic halos with a constant-density core of size r_h and secondly NFW halos (Navarro et al. 1996). The latter provide good fits to cosmological N-body simulations and have a central logarithmic slope of -1. Neither of the two profiles includes baryonic halo contraction explicitly (cf. the discussion in Sec. 5.2). Coma galaxies are in most cases better fit with logarithmic halos, but the significance over NFW halo profiles is marginal. The steeper central slope of NFW halos implies a higher central dark matter density. But even in cases where NFW halos fit better, the innermost galaxy regions are still dominated by the mass-component that follows the light (for details see Thomas et al. 2007b). The assumptions about the halo-density profile have therefore little influence on the best-fit stellar mass-to-light ratio $\Upsilon_{*,\rm dyn}$ (typically, $\Upsilon_{*,\rm dyn}$ from logarithmic or NFW halos differ by no more than $\Delta\Upsilon_{*,\rm dyn} \approx 0.5$; see also Sec. 4.2).

The gravitational potential of the galaxies is assumed to be axisymmetric. Contrasting other methods like using Jeans equations, the Schwarzschild technique allows the exploration of all possible orbit configurations. The Coma sample is unique in being the only larger sample of axisymmetric dynamical models including dark matter. Previous modelling attempts either assumed spherical symmetry (Gerhard et al. 2001) or did not include dark matter explicitly (Cappellari et al. 2006).

2.2 Stellar population models

Stellar ages, metallicities, [α/Fe] ratios and R-band stellar mass-to-light ratios are determined by fitting the single stellar population models of Maraston (1998, 2005) with α-elements overabundance of Thomas et al. (2003) to the Lick indices Hβ, $\langle$Fe$\rangle$, [MgFe] and Mg$\,b$. Two initial-stellar-mass functions are considered. Firstly, the Salpeter IMF ($\Upsilon_{\rm Salp}$, with mass limits of $0.1\,{\rm M}_\odot$ and $100\,{\rm M}_\odot$) and, secondly, the Kroupa IMF ($\Upsilon_{\rm Krou}$, with the same mass limits, but a shallower slope for stars below $0.5\,{\rm M}_\odot$). The Salpeter IMF implies more low-mass stars and a higher mass-to-light ratio. In the R-band the scaling between the two cases is $\Upsilon_{\rm Salp} \approx 1.56\,\Upsilon_{\rm Krou}$ (Salpeter 1955; Kroupa 2001). When the IMF does not need to be specified, we will refer to stellar-population mass-to-light ratios as $\Upsilon_{\rm ssp}$.

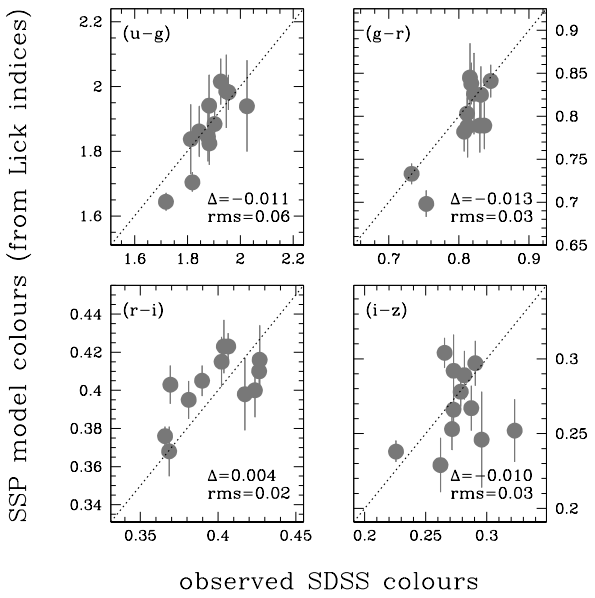

Figure 2. Observed versus predicted colours for the subsample of Coma galaxies with SDSS photometry. Colours as indicated in each panel. Model predictions are plotted along the vertical axis, SDSS observations horizontally. All axes are in magnitudes. The mean colour difference Δ and rms-scatter between models and observations (in magnitudes) is quoted in each panel.

Stellar population properties are calculated at each radius with observations. Salpeter R-band mass-to-light ratios are shown in Fig. 1. The light-weighted averages within $r_{\rm eff}$ are indicated by the dashed lines and form the basis for the remainder of this paper (Tab. 1). For some galaxies there are systematic differences between the two sides of a slit which are slightly larger than the statistical errors (e.g. along the major-axis of GMP0144). These systematic uncertainties are not included in the errors quoted in Tab. 1. Irrespective of the metalicity gradients present in early-type galaxies (Mehlert et al. 2003), mass-to-light ratio gradients in the R-band are generally small for the Coma galaxies (cf. Fig. 1). The results presented here do not depend significantly on the averaging radius. Its choice is driven by the most massive sample objects. Their spectroscopic data reach only out to $r_{\rm obs,max} \approx r_{\rm eff}$ and, for the purpose of homogeneity, we restrict the averaging in other galaxies to the same radius, even if the data extend further out.

For a subsample of the Coma galaxies studied here, multi-band photometry from the Sloan Digital Sky Survey (SDSS; York et al. 2000) is available. Fig. 2 compares observed SDSS colours with the predictions of our best-fit SSP models. We have applied the same colour corrections to the models as discussed in Saglia et al. (2010) plus an additional $i - z = -0.05$ (Maraston, private communication), to take

galaxy		$\Upsilon_{*,\rm dyn}$	$\Upsilon_{*,\rm sc}$	$f_{\rm DM,dyn}$	$\sigma_{\rm eff}$	$\Upsilon_{\rm Krou}$	$\Upsilon_{\rm Salp}$
GMP	NGC/IC	$[{\rm M}_\odot/{\rm L}_{R,\odot}]$	$[{\rm M}_\odot/{\rm L}_{R,\odot}]$		[km/s]	$[{\rm M}_\odot/{\rm L}_{R,\odot}]$	$[{\rm M}_\odot/{\rm L}_{R,\odot}]$
(1)	(2)	(3)	(4)	(5)	(6)	(7)	(8)
0144	4957	4.50 ± 0.50	7.00	$0.30^{+0.10}_{-0.05}$	211.8 ± 0.4	3.03 ± 0.17	4.74 ± 0.26
0282	4952	5.00 ± 0.50	6.50	$0.25^{+0.13}_{-0.05}$	268.2 ± 0.5	3.57 ± 0.22	5.58 ± 0.34
0756	4944	2.60 ± 0.20	3.00	$0.11^{+0.05}_{-0.05}$	193.2 ± 0.3	1.40 ± 0.06	2.19 ± 0.10
1176	4931	2.00 ± 0.20	2.50	$0.31^{+0.05}_{-0.04}$	205.6 ± 0.3	1.54 ± 0.04	2.41 ± 0.06
1750	4926	6.00 ± 0.75	7.00	$0.15^{+0.47}_{-0.05}$	279.1 ± 1.6	3.41 ± 0.50	5.33 ± 0.79
1990	IC 843	10.00 ± 1.00	10.00	$0.01^{+0.01}_{-0.01}$	281.3 ± 1.1	3.03 ± 0.30	4.74 ± 0.47
2417	4908	8.00 ± 0.75	8.50	$0.05^{+0.20}_{-0.04}$	211.0 ± 1.7	3.78 ± 0.43	5.91 ± 0.67
2440	IC 4045	6.50 ± 0.50	7.00	$0.07^{+0.02}_{-0.02}$	225.9 ± 0.9	3.46 ± 0.27	5.41 ± 0.42
3414	4871	4.00 ± 0.62	6.00	$0.46^{+0.06}_{-0.27}$	169.6 ± 1.3	3.20 ± 0.29	4.99 ± 0.45
3510	4869	5.50 ± 0.50	6.00	$0.09^{+0.18}_{-0.05}$	177.7 ± 1.7	3.49 ± 0.65	5.45 ± 1.02
3792	4860	8.00 ± 1.00	9.00	$0.13^{+0.24}_{-0.05}$	284.0 ± 1.9	4.27 ± 0.31	6.66 ± 0.48
4822	4841A	5.50 ± 1.00	6.50	$0.51^{+0.14}_{-0.27}$	272.1 ± 2.7	3.24 ± 0.33	5.07 ± 0.52
4928	4839	8.50 ± 2.00	10.00	$0.32^{+0.35}_{-0.21}$	314.8 ± 2.9	3.34 ± 0.46	5.22 ± 0.72
5279	4827	6.50 ± 0.50	7.00	$0.10^{+0.21}_{-0.07}$	244.1 ± 1.2	3.16 ± 0.45	4.93 ± 0.71
5568	4816	6.00 ± 1.00	7.00	$0.53^{+0.15}_{-0.25}$	233.4 ± 1.7	3.91 ± 0.33	6.11 ± 0.52
5975	4807	3.00 ± 0.50	4.00	$0.29^{+0.05}_{-0.01}$	195.9 ± 0.8	3.07 ± 0.24	4.80 ± 0.37

Table 1. Dynamical parameters of Coma galaxies. (1, 2) galaxy identification (GMP from Godwin et al. 1983). (3) best-fit dynamical $\Upsilon_{*,\rm dyn}$ (R-band) in models that explicitly account for dark matter (the quoted errors include all models that deviate by less than $\Delta\chi^2 \leqslant 1$ from the best-fit model. For a more detailed discussion of the errors the reader is referred to Thomas et al. 2005a.) (4) best-fit dynamical $\Upsilon_{*,\rm sc}$ (R-band) assuming that all the mass follows the light. (According to Fig. 2 in Thomas et al. 2007b the formal errors on $\Upsilon_{*,\rm sc}$ are smaller than those of $\Upsilon_{*,\rm dyn}$. However, since the assumption that mass-follows-light does not yield satisfactory fits to the kinematics we don't give errors for $\Upsilon_{*,\rm sc}$ here.) (5) dark matter fraction $f_{\rm DM,dyn}$ within $r_{\rm eff}$. (6) galaxy velocity dispersion $\sigma_{\rm eff}$ (inside $r_{\rm eff}$). (7, 8) stellar population mass-to-light ratios for the Kroupa IMF ($\Upsilon_{\rm Krou}$; R-band) and Salpeter IMF ($\Upsilon_{\rm Salp}$; R-band), respectively. The mass-to-light ratios are light-weighted averages within $r_{\rm eff}$. Only radii with a stellar-population age $\tau \leqslant 14\,{\rm Gyr}$ are considered.

into account the recent improvements in the calibration of the Maraston SSP models (Maraston et al. 2009). The vertical error-bars indicate the 68% confidence region derived from the observational errors. Model colours are averaged inside $r_{\rm eff}$. They fit well to the SDSS colours with average differences smaller than $\lesssim 0.01$ mag.

Grillo & Gobat (2010) used observed SDSS colours to derive photometric stellar population parameters for some of our Coma galaxies. In contrast to the analysis presented here, they (1) assume a solar metallicity for all galaxies (but see the middle panel of Fig. 11) (2) allow for an extended star-formation history and (3) use the Maraston (2005) models without colour corrections. In Fig. 3 we plot their photometric $\Upsilon^{\rm SDSS}_{\rm Krou}$ (scaled to the Kroupa IMF) against our $\Upsilon_{\rm Krou}$. On average, both approaches yield consistent results ($\langle\Upsilon_{\rm Krou}/\Upsilon^{\rm SDSS}_{\rm Krou}\rangle = 1.11$), though the rms-scatter (± 0.35) is large.

3 PROJECTED MASSES FROM DYNAMICS AND LENSING

As it has been stated in Sec. 1, the dynamical models rely on the assumption of axial symmetry and steady state dynamics. To check how accurately these assumptions are fulfilled in real galaxies we first compare our dynamical models against gravitational lensing results. The latter constrain the total projected mass inside a cylinder delimited by the Einstein radius $r_{\rm Ein}$ of the lens and are less affected by symmetry assumptions (Kochanek 1991).

3.1 Lens selection

The Einstein radius of a gravitational lens results from two independent properties of a lensing configuration. Firstly, from the physical deflection angle that the lensing galaxy gives rise to according to its gravity. It depends only on the mass distribution of the foreground galaxy. Secondly, from projection factors that depend on the distances of the foreground lens and the background source, respectively. For the Coma galaxies we only know their mass distributions, but they are not part of real lenses. To compare them with observed gravitational lenses, we need to define an appropriate lensing configuration for each Coma galaxy. Here we do this implicitly by seeking for lensing galaxies that accidentally happen to fall on a linear relation $r_{\rm Ein}(\sigma_{\rm eff})$ between the Einstein radius and the effective velocity dispersion. Defining a fiducial Einstein radius for each Coma galaxy according to the same $r_{\rm Ein}(\sigma_{\rm eff})$ then ensures, that there is at least a subsample of real lenses with similar lens configurations at a given $\sigma_{\rm eff}$. The Coma galaxies can be compared to the lenses in such a subsample, but not to the rest of the lensing galaxies. The form of the selection function is arbitrary, any other function would serve equally well. We choose a linear relation for simplicity.

Fig. 4 shows the observed Einstein radii $r_{\rm Ein}$ of SLACS lenses from Auger et al. (2009) against their velocity dispersions[1]. The large circles show two different subsamples

[1] Note that for Fig. 4 we have used the correction of

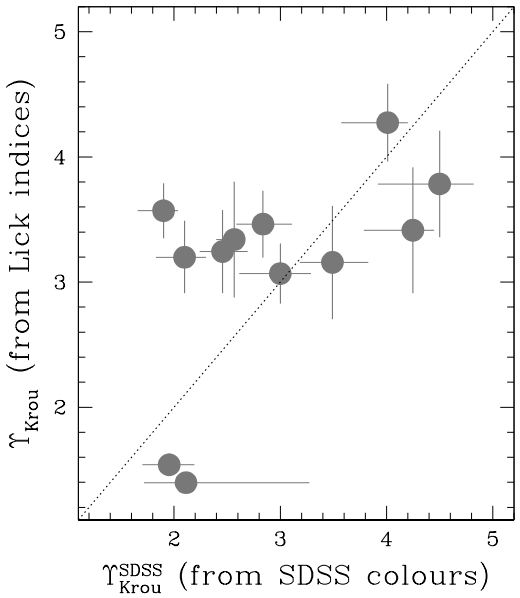

Figure 3. Stellar population $\Upsilon_{\rm Krou}$ (Kroupa IMF) from SDSS colours (x-axis; cf. Grillo & Gobat 2010) and from Lick indices (y-axis; cf. Tab. 1).

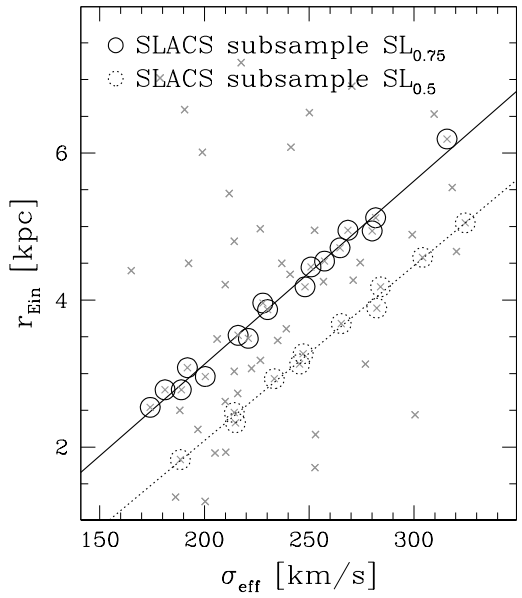

Figure 4. Einstein radii $r_{\rm Ein}$ and effective velocity dispersions $\sigma_{\rm eff}$ of SLACS galaxies from Auger et al. (2009) are shown by the crosses. Dotted open circles highlight lenses that follow eq. (4), shown by the dotted line, and form subsample $SL_{0.5}$; solid open circles are for subsample $SL_{0.75}$ (i.e. galaxies that follow eq. 5, shown by the solid line).

of lenses constructed as outlined above. The lenses are selected to deviate by less than 0.2 kpc from two arbitrary linear selection functions $r_{\rm Ein}(\sigma_{\rm eff}) = 0.025\,\sigma_{\rm eff} - 3.0$ and $r_{\rm Ein}(\sigma_{\rm eff}) = 0.025\,\sigma_{\rm eff} - 1.9$. After having selected the lenses we fit a straight line to each subsample in order to determine the actual best-fit $r_{\rm Ein}(\sigma_{\rm eff})$ that is used to define fiducial Einstein radii for Coma galaxies. The fitted relations differ only slightly from the original selection functions. For subsample $SL_{0.5}$ (dotted) we get

$$\frac{r_{\rm Ein}}{\rm kpc} = 0.0238 \times \frac{\sigma_{\rm eff}}{\rm km/s} - 2.6709 \qquad (4)$$

and for subsample $SL_{0.75}$ (solid)

$$\frac{r_{\rm Ein}}{\rm kpc} = 0.0249 \times \frac{\sigma_{\rm eff}}{\rm km/s} - 1.8564. \qquad (5)$$

The two subsamples are constructed as a compromise between (1) ending up with a sizeable number of galaxies in each subsample and (2) yielding sufficiently different subsamples to allow for a comparison between Coma and lensing galaxies at different physical scales. For subsample $SL_{0.5}$ we get an average $\langle r_{\rm Ein}/r_{\rm eff}\rangle \approx 0.5$ (11 lenses), while for subsample $SL_{0.75}$ it is $\langle r_{\rm Ein}/r_{\rm eff}\rangle \approx 0.75$ (17 lenses).

3.2 The total mass

The large symbols in Fig. 5 show projected, integrated masses of Coma galaxies and SLACS lenses as a function of galaxy velocity dispersion $\sigma_{\rm eff}$. Coma masses are calculated from the integral

$$M_{\rm Ein} \equiv \int_{-10\,r_{\rm eff}}^{10\,r_{\rm eff}} {\rm d}z \int_0^{2\pi} {\rm d}\varphi \int_0^{r_{\rm Ein}(\sigma_{\rm eff})} \rho\, r\, {\rm d}r, \qquad (6)$$

Cappellari et al. (2006) to transform the measured SDSS aperture dispersions into $\sigma_{\rm eff}$.

where (r, φ) are polar coordinates on the sky and z is the direction of the line-of-sight. Formally, the integral in eq. (6) should be calculated over $-\infty \leqslant z \leqslant +\infty$, but we limited it over $-10\,r_{\rm eff} \leqslant z \leqslant +10\,r_{\rm eff}$. For an isothermal sphere this cut-off results in a negligible underestimation of the integral ($\approx 4\,\%$). Coma galaxy velocity dispersions $\sigma_{\rm eff}$ are measured by (1) reconstructing the line-of-sight velocity distributions (LOSVDs) from the kinematic moments, (2) coadding all LOSVDs inside $r_{\rm eff}$, each weighted by its projected light, and (3) fitting a Gaussian to the resulting LOSVD. They are listed in Tab. 1. Because of their higher signal-to-noise, only the major-axis data have been considered. The upper integration limit $r_{\rm Ein}(\sigma_{\rm eff})$ in eq. (6) refers to eq. (4) for the comparison with SLACS subsample $SL_{0.5}$ and to eq. (5) for the comparison with subsample $SL_{0.75}$. In Fig. 5 we only show those SLACS lenses that belong to either subsample $SL_{0.5}$ (left-hand panels) or subsample $SL_{0.75}$ (right-hand panels), respectively.

The top row is for the total cylindrical mass of our standard two-component models with dark matter halos (i.e. with the best-fit density $\rho = \Upsilon_{*,\rm dyn} \times \nu + \rho_{\rm DM,dyn}$ in eq. 6). The good agreement with the lensing results is reassuring (the average mass offset is 0.05 dex for subsample $SL_{0.5}$ and 0.02 dex for subsample $SL_{0.75}$). It implies that the two completely independent methods yield consistent results. Moreover, the scatter in the dynamical masses is not larger than in the lensing masses. Consequently, strong deviations from axisymmetry are unlikely in the Coma galaxies. As shown in Thomas et al. (2007a), strong triaxiality, if not accounted for in the models, can bias dynamical masses by a factor of up to two, depending on viewing angle. Assuming random viewing angles, strongly triaxial mass distribu-

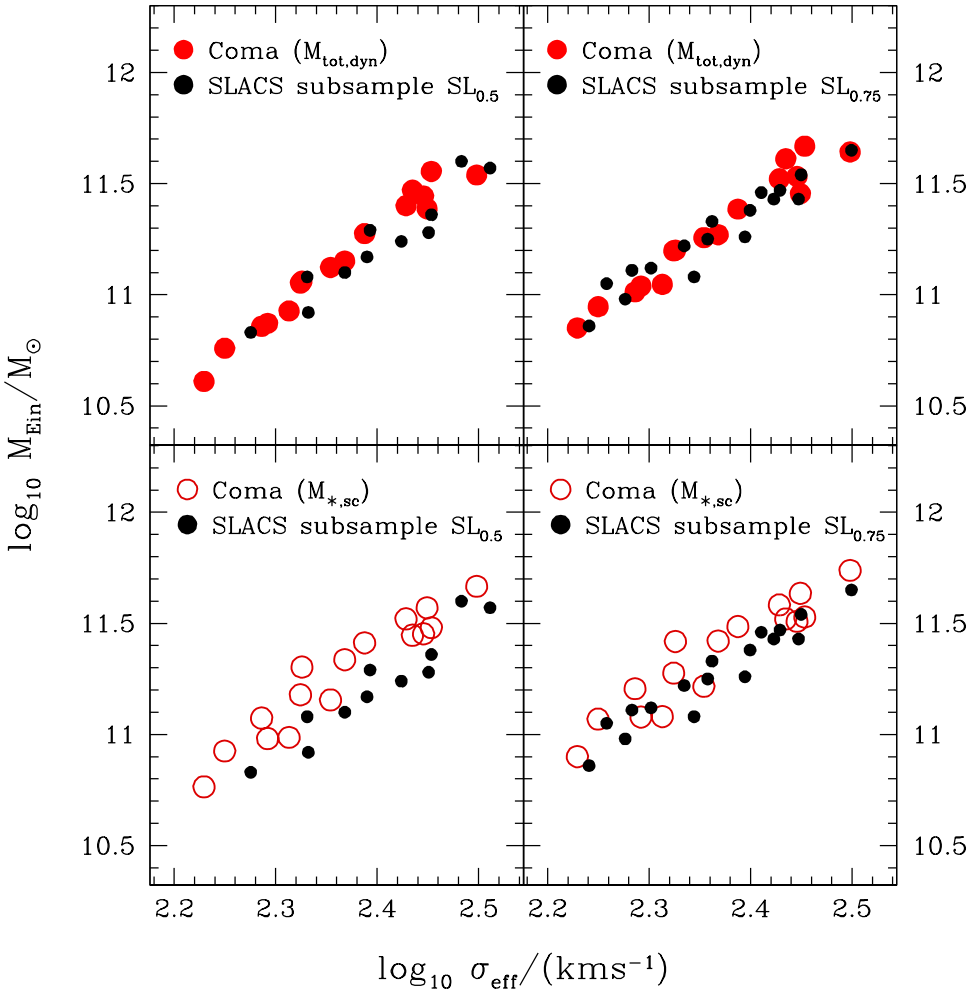

Figure 5. The projected total (luminous+dark) mass $M_{\rm Ein}$ within a fiducial Einstein radius $r_{\rm Ein}$. Coma galaxies are indicated by the large symbols. Top row: two-component models with dark matter halos ($\rho = \Upsilon_{*,\rm dyn} \times \nu + \rho_{\rm DM,dyn}$ in equation 6); bottom row: dynamical mass under the assumption that mass follows light ($\rho = \Upsilon_{*,\rm sc} \times \nu$). Small circles: total projected masses of SLACS galaxies (Auger et al. 2009). In the left-hand panels we compare Coma galaxies with the SLACS subsample $SL_{0.5}$ using fiducial Einstein radii calculated via eq. (4). In the right-hand panels we compare to subsample $SL_{0.75}$ (using eq. 5). Masses are plotted against the average velocity dispersion $\sigma_{\rm eff}$ inside $r_{\rm eff}$.

tions would therefore likely cause a significant scatter in the dynamical masses, which is however not observed (but see van de Ven, Mandelbaum, & Keeton 2009).

The bottom row of Fig. 5 is for projected masses of self-consistent dynamical models in which all the mass is assumed to follow the light (i.e. $\rho = \Upsilon_{*,\rm sc} \times \nu$). These models are not consistent with the lensing masses. The discrepancy is larger for the SLACS subsample $SL_{0.5}$ than for subsample $SL_{0.75}$ because the smaller Einstein radii of subsample $SL_{0.5}$ emphasise the central regions in the comparison. As it has been shown earlier (e.g. Gerhard et al. 2001, Thomas et al. 2007b), the mass distribution in early-type galaxies follows the light in the inner regions ($\rho_{\rm in} \approx \Upsilon_{*,\rm dyn} \times \nu_{\rm in}$), but has an additional component in the outer parts ($\rho_{\rm out} \approx \Upsilon_{*,\rm dyn} \times \nu_{\rm out} + \rho_{\rm DM}$). Then, assuming that all the mass follows the light requires $\Upsilon_{*,\rm sc} > \Upsilon_{*,\rm dyn}$ to include the outer dark matter ($\Upsilon_{*,\rm sc} \times \nu_{\rm out} \approx \rho_{\rm out} \approx \Upsilon_{*,\rm dyn} \times \nu_{\rm out} + \rho_{\rm DM}$). However, the central regions become proportionally more massive, too, such that $\Upsilon_{*,\rm sc} \times \nu_{\rm in} > \Upsilon_{*,\rm dyn} \times \nu_{\rm in} \approx \rho_{\rm in}$. This explains why the offset in the lower-left panel of Fig. 5 is larger than in the lower-right one.

3.3 Stellar population masses

In Fig. 6 we show projected *stellar* masses (i.e. using $\rho = \Upsilon_{\rm Salp} \times \nu$ and $\rho = \Upsilon_{\rm Krou} \times \nu$, respectively, in eq. 6). The open dots in these panels represent the projected *stellar* masses for either the Salpeter IMF (top row) or the Kroupa IMF (bottom row). Kroupa stellar masses are always below lensing masses. The mass difference between the lenses and the Kroupa masses increases from subsample $SL_{0.5}$ to subsample $SL_{0.75}$ for the same reason discussed at the end of Sec. 3.2.

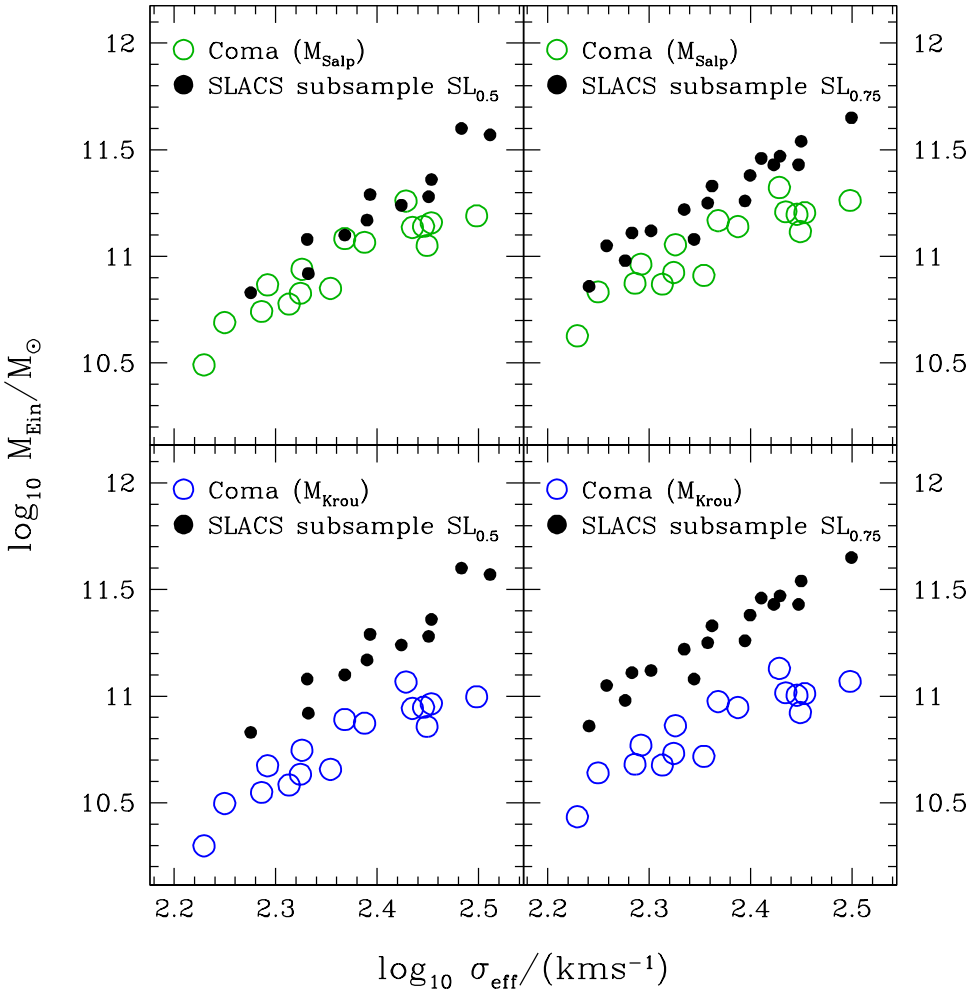

Figure 6. As Fig. 5, but for stellar population masses. Top row: Salpeter IMF ($\rho = \Upsilon_{\rm Salp} \times \nu$); bottom row: Kroupa IMF ($\rho = \Upsilon_{\rm Krou} \times \nu$).

It could be due to dark matter. Salpeter stellar masses are likewise consistent with the lensing results. In low-dispersion galaxies the IMF cannot be much steeper than Salpeter as otherwise the implied stellar masses would exceed the total observed lens masses. In high-dispersion galaxies the Salpeter stellar masses are however not enough to explain the total lensing masses. Then, if all the lensing mass was stellar, the IMF would have to change with galaxy velocity dispersion and in massive early-types the stellar mass per stellar light would have to be larger than for a Salpeter IMF (or any equivalent top-heavy IMF). If the IMF is constant, then the top-left panel of Fig. 6 provides direct evidence for the presence of dark matter in high-dispersion early-type galaxies.

3.4 Luminous and dark matter separated

In our standard two-component models that take into account the detailed, radially resolved stellar kinematics, the large projected masses of high-dispersion galaxies do not entirely originate from luminous mass. This is shown in the top panel of Fig. 7 (projected dark matter fractions inside the Einstein radius). Note that here we compare to the results of Koopmans et al. (2006), who provided a combined lensing and dynamics analysis of the first SLACS galaxies. We applied a similar lens selection as described in Sec. 3.1 (using $r_{\rm Ein} = 0.03244 \times \sigma_{\rm eff} - 4.6324$). Our dynamically derived dark matter fractions are in good agreement with those from Koopmans et al. (2006). As already stated above, they increase with $\sigma_{\rm eff}$. For comparison, we have also plotted the corresponding deprojected dark matter fractions (cf. eq. 3) inside the same three dimensional radius $r_{\rm Ein}(\sigma_{\rm eff})$ in the bottom panel of Fig. 7. They are generally lower and do not vary with $\sigma_{\rm eff}$. Projection effects therefore contribute to the trends in Figs. 5-7. To get a better understanding about the stellar IMF and dark matter distribution it is necessary to analyse the intrinsic three dimensional properties of the galaxies. This will be done in the following Secs. 4 and 5.

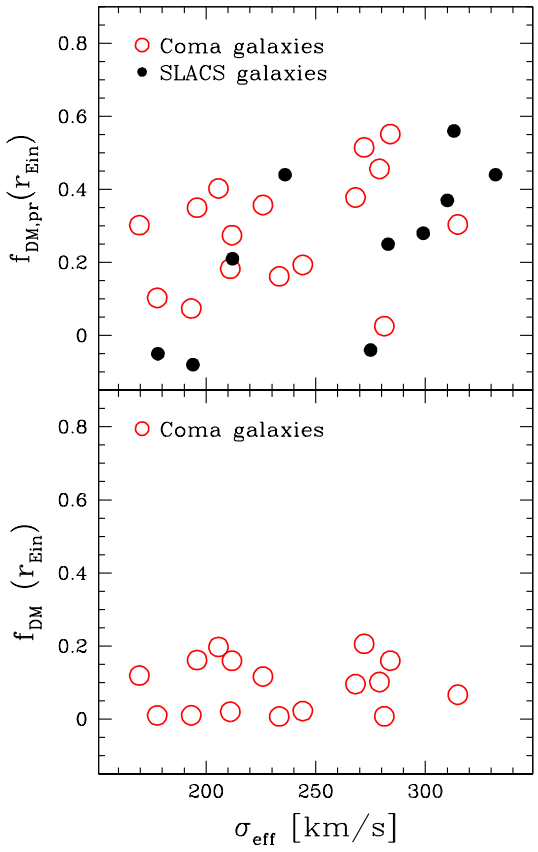

Figure 7. Dark matter fractions inside the Einstein radius. Top: projected dark matter fraction; bottom: deprojected dark matter fraction. Red/open circles: Coma galaxies of this work; dark/filled circles in the top panel: SLACS galaxies from Koopmans et al. (2006). Coma galaxy dark matter fractions are plotted against the velocity dispersion $\sigma_{\rm eff}$ inside $r_{\rm eff}$. SLACS galaxies are plotted against the measured velocity dispersion inside the SDSS aperture.

4 DYNAMICAL LUMINOUS MASS VERSUS STELLAR POPULATION MASS

Fig. 8 shows dynamical and stellar-population mass-to-light ratios versus $\sigma_{\rm eff}$. The dynamical $\Upsilon_{*,\rm dyn}$ exhibit a broad distribution ranging from $\Upsilon_{*,\rm dyn} \approx 2$ to $\Upsilon_{*,\rm dyn} \approx 10$. In contrast, for the majority of Coma galaxies the stellar population $\Upsilon_{\rm ssp}$ are almost constant with $\Upsilon_{\rm Salp} \approx 5-6$ for the Salpeter IMF and $\Upsilon_{\rm Krou} \approx 3-4$ for the Kroupa IMF. In addition, while the dynamical $\Upsilon_{*,\rm dyn}$ clearly increase with galaxy velocity dispersion, there is no similar correlation between $\sigma_{\rm eff}$ and stellar-population $\Upsilon_{\rm ssp}$.

There are two galaxies (GMP0756 and GMP1176) with distinctly lower stellar mass-to-light ratios than in the rest of the sample. As Fig. 9 shows, these two galaxies have overall young stellar populations. In general, one can read off from Figs. 8 and 9 that dynamical $\Upsilon_{*,\rm dyn}$ depend on $\sigma_{\rm eff}$ but not primarily on the stellar population age, while $\Upsilon_{\rm ssp}$ mostly reflect stellar ages and do not show any dependency on $\sigma_{\rm eff}$.

4.1 Variation in the stellar IMF?

Since dynamical and stellar population masses scale differently with galaxy velocity dispersion (cf. Fig. 8), the ratio $\Upsilon_{*,\rm dyn}/\Upsilon_{\rm ssp}$ has to vary with galaxy $\sigma_{\rm eff}$ (for any fixed IMF). This is explicitly shown by the large/red symbols in Fig. 10. In addition to our results, the figure also combines work from other groups.

Pentagons represent the stellar-population analysis of a subsample of our Coma galaxies by Grillo & Gobat (2010) (cf. Sec. 2.2). The pentagons differ from the large filled symbols only in terms of $\Upsilon_{\rm Krou}$. The velocity dispersions and dynamical $\Upsilon_{*,\rm dyn}$ are the same.

Triangles are for the SAURON survey (Cappellari et al. 2006). In terms of both, the stellar population analysis (based on spectral absorption line indices) as well as the dynamical modelling (orbit-based), they can be most directly compared to the Coma galaxies of this work. Note, however, that Cappellari et al. (2006) measured only the sum of luminous and dark mass, assuming the latter to contribute only a small amount of mass in the central galaxy regions observed with SAURON ($r_{\rm obs,max} \lesssim r_{\rm eff}$). Adopting equivalent modelling assumptions for the Coma galaxies yields mass-to-light ratios typically $10-20\,\%$ higher than compared with stellar $\Upsilon_{*,\rm dyn}$ from models where dark matter is accounted for explicitly (cf. Tab. 1). The overall distributions of $\Upsilon_{*,\rm dyn}/\Upsilon_{\rm Krou}$ are nevertheless similar in both samples.

Finally, Fig. 10 also includes SLACS galaxies, analysed with a combined dynamics and lensing approach (Treu et al. 2010). For these galaxies, the ratio of the total versus the stellar mass (the latter derived from broad-band colours) inside the Einstein radius (typically of the order of $r_{\rm eff}/2$) is plotted along the y-axis.

In all the samples included in Fig. 10 dynamical (or lensing) stellar masses systematically exceed the required masses for a Kroupa IMF. Above $\sigma_{\rm eff} \gtrsim 150\,$km/s the ratio $\Upsilon_{*,\rm dyn}/\Upsilon_{\rm Krou}$ tends to increase with velocity dispersion. For lower mass galaxies the ratio becomes uncertain due to the more frequent presence of multiple stellar populations (e.g. Cappellari et al. 2006). Moreover, for low-mass galaxies the assumption that all the mass follows the light is in conflict with gravitational lensing masses (cf. Sec. 3).

If the increase of $\Upsilon_{*,\rm dyn}/\Upsilon_{\rm Krou}$ with $\sigma_{\rm eff}$ was a pure stellar population effect then we would have to assume that the IMF is not universal. Interpreted in this way, Fig. 10 would imply the IMF in high-dispersion galaxies to produce either more low-mass stars than the Kroupa IMF (i.e. being Salpeter-like) or more stellar remnants (i.e. being top-heavy). A higher fraction of low-mass stars would reduce the number of SNe of type II (per stellar mass) and would lead to an overall lower metallicity. Thus, if the IMF changed from Kroupa towards Salpeter, then the increase in $\Upsilon_{*,\rm dyn}/\Upsilon_{\rm Krou}$ would be expected to come along with a decrease in [Z/H]. Instead, a top-heavy IMF enhances the importance of type II SNe over type Ia SNe. Accordingly, if the IMF changed from Kroupa towards being top-heavy then one would expect higher [α/Fe] in galaxies with higher $\Upsilon_{*,\rm dyn}/\Upsilon_{\rm Krou}$ (Thomas, Greggio, & Bender 1999; Graves & Faber 2010).

Fig. 11 shows $\Upsilon_{*,\rm dyn}/\Upsilon_{\rm Krou}$ against stellar population age τ, metallicity [Z/H] and [α/Fe] ratio. There is no correlation with any stellar population parameter. Note, however,

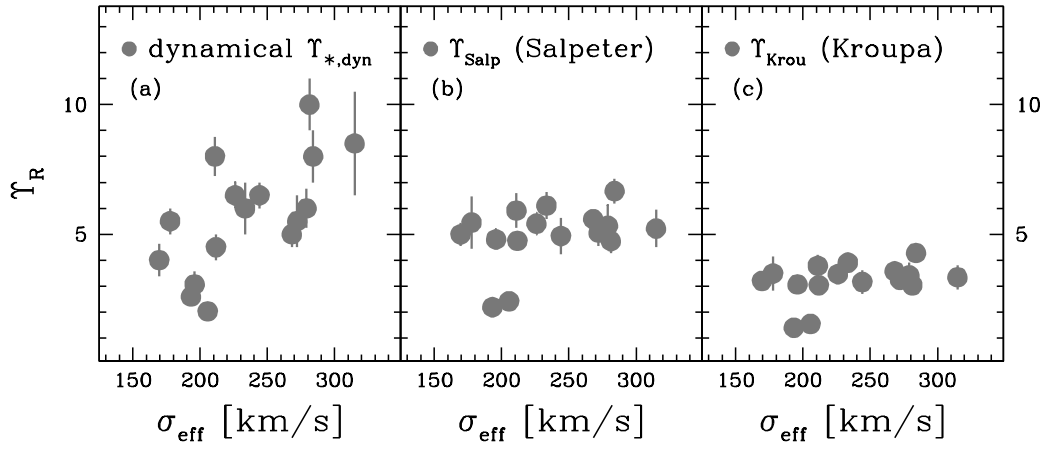

Figure 8. Stellar mass-to-light ratios (R-band) against average velocity dispersion $\sigma_{\rm eff}$ inside $r_{\rm eff}$. From left-to-right: a) dynamical $\Upsilon_{*,\rm dyn}$, b) stellar-population $\Upsilon_{\rm Salp}$ for the Salpeter IMF and c) stellar-population $\Upsilon_{\rm Krou}$ for the Kroupa IMF. Circles: E/S0 and S0 galaxies; squares: ellipticals.

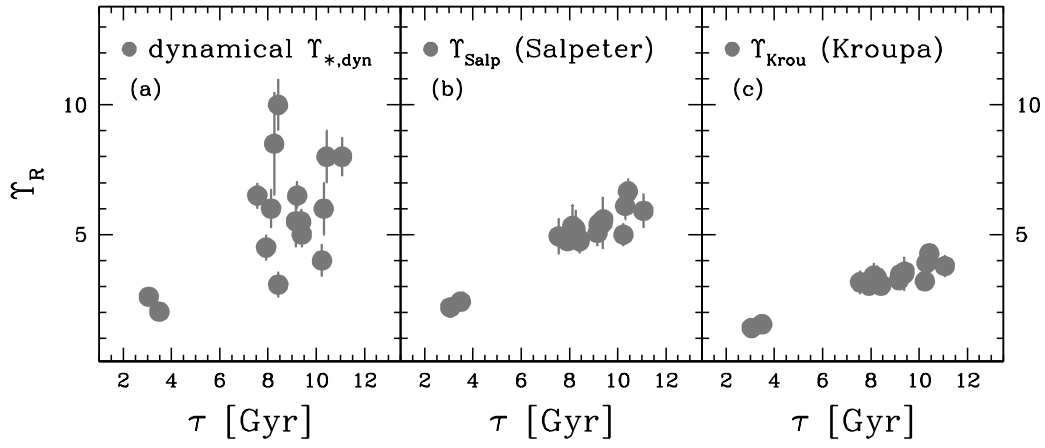

Figure 9. As Fig. 8, but stellar mass-to-light ratios are plotted against stellar population age τ.

that stellar metallicities and [α/Fe] ratios do not only depend on the stellar IMF, but also on the duration of the star-formation episode(s), the depth of the galaxy potential well and on evolutionary processes related to the cluster environment. In this respect, the lack of evidence for an IMF change cannot be taken as a proof for a constant IMF. Alternatives to IMF variation are discussed in Secs. 4.4 and 5.2.

4.2 The shape of the stellar IMF

A direct comparison between dynamical and stellar-population mass-to-light ratios is provided by Fig. 12. As already clear from the different scalings of $\Upsilon_{*,\rm dyn}$ on the one side and $\Upsilon_{\rm ssp}$ on the other (cf. Figs. 8 and 9), neither the Kroupa IMF nor the Salpeter IMF yields a close match between $\Upsilon_{*,\rm dyn}$ and $\Upsilon_{\rm ssp}$.

Above the dotted line in Fig. 12 the luminous dynamical mass is larger than the stellar mass required for the Kroupa IMF, while below the line the dynamical $\Upsilon_{*,\rm dyn}$ is formally insufficient for the Kroupa IMF. For the Salpeter IMF the corresponding limit is shifted towards $\Upsilon_{*,\rm dyn}$ which are a factor 1.6 higher (dashed line). Accordingly, all Coma galaxies are compatible with a Kroupa IMF. The majority of the galaxies is also consistent with a Salpeter IMF, but there is at least one galaxy for which the dynamical $\Upsilon_{*,\rm dyn}$ is significantly lower than $\Upsilon_{\rm Salp}$ (at about the $3\,\sigma$ level; GMP5975). Concerning the total sample, however, the Salpeter IMF fits the dynamical masses better than the Kroupa IMF. The corresponding sample averages are $\langle\Upsilon_{*,\rm dyn}/\Upsilon_{\rm Salp}\rangle = 1.15$ for the Salpeter IMF (with an rms scatter of 0.35) and $\langle\Upsilon_{*,\rm dyn}/\Upsilon_{\rm Krou}\rangle = 1.8$ for the Kroupa IMF, respectively.

These conclusions also hold for other galaxy samples. Since $\Upsilon_{\rm Salp} \approx 1.6 \times \Upsilon_{\rm Krou}$, the one-to-one line for the Salpeter IMF in Fig. 10 would occur at $\Upsilon_{*,\rm dyn}/\Upsilon_{\rm ssp} \approx 1.6$. Then, the Salpeter IMF provides *on average* a better match with dynamical/lensing masses. In line with this, recent near-infrared spectroscopic observations point towards a bottom-heavy IMF in massive early-type galaxies as well (van Dokkum & Conroy 2010, 2011). However, our dynamical models as well as previous lensing studies (Ferreras et al. 2010; Treu et al. 2010) indicate that around $\sigma_{\rm eff} \lesssim 200\,$km/s

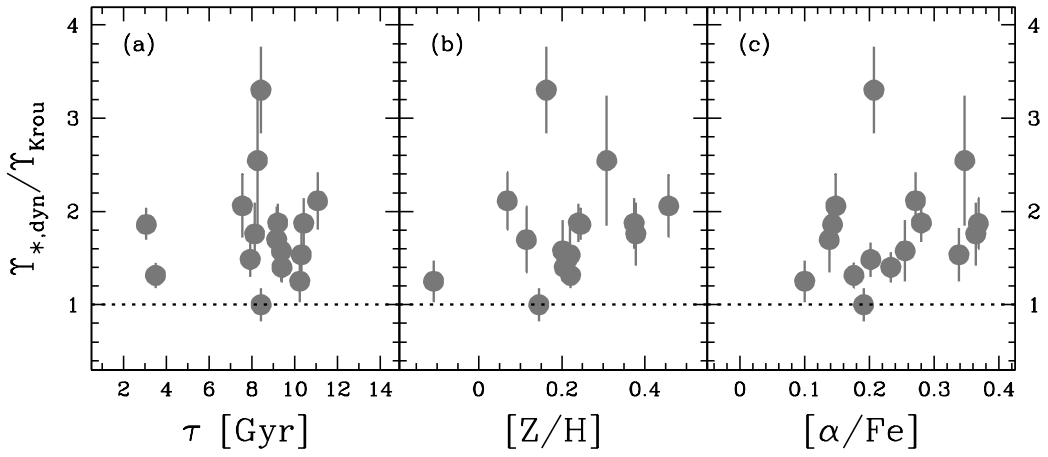

Figure 11. Ratio $\Upsilon_{*,\rm dyn}/\Upsilon_{\rm Krou}$ against stellar population age τ (panel a), metallicity [Z/H] (panel b) and abundance ratio [α/Fe] (panel c).

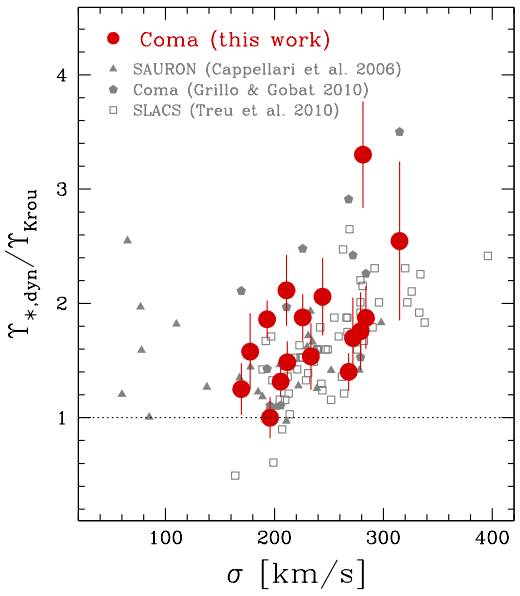

Figure 10. Ratio $\Upsilon_{*,\rm dyn}/\Upsilon_{\rm Krou}$ versus velocity dispersion σ. Large, filled: spectroscopic $\Upsilon_{\rm Krou}$ and orbit-based dynamical models accounting for dark matter (this work); triangles: spectroscopic $\Upsilon_{\rm Krou}$ and orbit-based dynamical models neglecting dark matter (Cappellari et al. 2006); pentagons: photometric $\Upsilon_{\rm Krou}$ (Grillo & Gobat 2010) and orbit-based dynamical models accounting for dark matter; open squares: photometric $\Upsilon_{\rm Krou}$ and combined lensing + dynamics models (Treu et al. 2010). For all but the SLACS galaxies the average velocity dispersion $\sigma_{\rm eff}$ inside $r_{\rm eff}$ is plotted. The SLACS dispersions are the average over the spectroscopic aperture of the SDSS survey.

the Salpeter stellar masses exceed the observed dynamical and/or lensing limits. This rules out a Salpeter IMF for low-mass galaxies.

The results for the Coma galaxies are largely independent of the parameterisation chosen for the dark matter halos. Fits with logarithmic halos alone yield $\langle\Upsilon^{\rm LOG}_{*,\rm dyn}/\Upsilon_{\rm Salp}\rangle = 1.16$, while NFW halos result in $\langle\Upsilon^{\rm NFW}_{*,\rm dyn}/\Upsilon_{\rm Salp}\rangle = 1.06$. Both are consistent within the rms scatter (about ≈ 0.32).

4.3 Uncertainties in population $\Upsilon_{\rm ssp}$

Gas emission can refill the Hβ line and lead to an overestimate of stellar population ages and, then, of $\Upsilon_{\rm ssp}$. A young stellar subpopulation (dominating in terms of light, but not in mass) can likewise bias stellar ages and $\Upsilon_{\rm ssp}$, yet towards too low values. In any case, $\Upsilon_{*,\rm dyn}/\Upsilon_{\rm ssp}$ would systematically decrease with stellar population age. Fig. 11a shows however, that this is not the case in the Coma galaxies, such that a strong bias due to gas emission or young stellar subpopulations is unlikely.

The stellar population parameters of the Coma galaxies are derived from spectral indices and, thus, represent averages along the line-of-sight. In other words, at a given radius of observation $r_{\rm obs}$, the SSP parameters combine the properties of stars with $r > r_{\rm obs}$. In contrast, dynamical models are most sensitive to the mass distribution inside $r_{\rm obs}$. Projection effects can therefore introduce a systematic bias between dynamical $\Upsilon_{*,\rm dyn}$ and stellar population $\Upsilon_{\rm ssp}$ if the stellar-population changes with radius. A monotonic stellar population gradient is enhanced after projection along the line-of-sight but diminished in the cumulative mass-to-light ratio constrained by dynamical models (Thomas 2006). More specifically, a radial increase of Υ leads to an underestimation of $\Upsilon_{*,\rm dyn}/\Upsilon_{\rm ssp}$, a radial decrease of Υ to an overestimation of $\Upsilon_{*,\rm dyn}/\Upsilon_{\rm ssp}$. For a rather steep gradient of $\mathrm{d}\log\Upsilon/\mathrm{d}\log r = \pm 0.23$ (a change by a factor of 1.7 per decade in radius), the expected systematic difference between $\Upsilon_{*,\rm dyn}$ and $\Upsilon_{\rm ssp}$ would amount to ∓ 30 percent inside $r_{\rm eff}$ (Thomas 2006). The observed gradients in the Coma galaxies are however much smaller (cf. Fig. 1). Therefore systematics due to projection effects seem negligible.

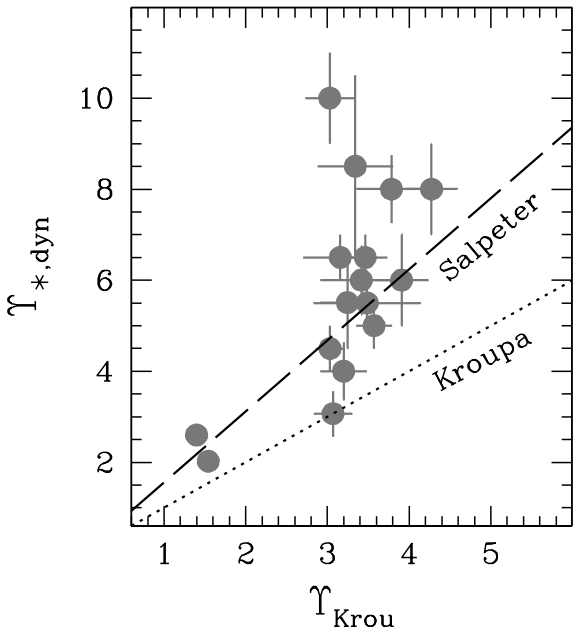

Figure 12. Dynamical $\Upsilon_{*,\rm dyn}$ versus stellar-population mass-to-light ratio $\Upsilon_{\rm Krou}$. The dotted line shows the one-to-one relation for the Kroupa IMF. Since $\Upsilon_{\rm Salp} = 1.56 \times \Upsilon_{\rm Krou}$, the corresponding one-to-one relation for the Salpeter IMF occurs at larger $\Upsilon_{*,\rm dyn}$ (dashed line).

4.4 Uncertainties and interpretation of dynamical $\Upsilon_{*,\rm dyn}$

The dynamical mass-to-light ratios $\Upsilon_{*,\rm dyn}$ could be affected by systematic biases in the modelling process, e.g. arising from false symmetry assumptions. As it has been stated in Sec. 1 the luminous $\Upsilon_{*,\rm dyn}$ can be biased by a factor of up to two, if the studied galaxies deviate significantly from the symmetry assumed in our models (Thomas et al. 2007a). However, there is no evidence for the Coma galaxies to be strongly non-axisymmetric. Firstly, they do not show significant isophotal twists as would be indicative for triaxiality. Secondly, as already discussed in Sec. 3, the good match between dynamical and strong-lensing masses provides further evidence that the obtained dynamical masses are unbiased.

Even if the luminous $\Upsilon_{*,\rm dyn}$ are accurate, they might not represent the galaxy *stellar* mass in a one-to-one fashion. Ambiguities can come from any non-stellar mass that follows the light and contributes to $\Upsilon_{*,\rm dyn}$.

Such a mass component could be gas loss during stellar evolution. It is not included in our $\Upsilon_{\rm ssp}$, which only encompass the baryonic mass locked in stars or stellar remnants. For a 10 Gyr old population the lost gas mass amounts to about 40 percent of the originally formed stellar mass (e.g. Maraston 2005). Provided that it remains in the galaxies and provided it follows the light distribution, it would contribute to the dynamical mass $\Upsilon_{*,\rm dyn}$ and the actual baryonic mass in stars and stellar remnants would only be $(f_* \Upsilon_{\rm dyn}) \times L$ (with $f_* \approx 0.6$). Correcting the dynamical $\Upsilon_{*,\rm dyn}$ for stellar mass loss yields formally a good agreement with the Kroupa IMF: $\langle (f_* \Upsilon_{\rm dyn}) / \Upsilon_{\rm Krou} \rangle = 1.04 \pm 0.32$.

Theoretical arguments indicate that most of the lost gas is either expelled from the galaxies or recycled into new stars. Only a few percent of the original stellar mass is expected to remain in hot gas halos around the galaxies (e.g. Ciotti et al. 1991; David et al. 1991). Fittingly, observed gas mass fractions of hot X-ray halos around massive early-type galaxies are typically less than a percent of the present stellar mass (e.g. Matsushita 2001), such that stellar mass loss is unlikely to explain the excess $\Upsilon_{*,\rm dyn} > \Upsilon_{\rm Krou}$.

A possible component of non-baryonic matter that follows the light is discussed below in Sec. 5.2.

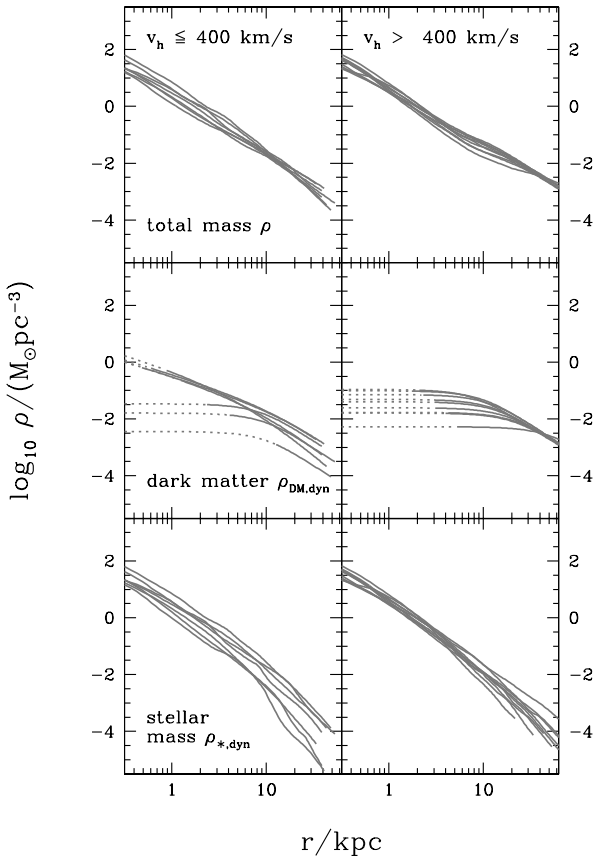

Figure 13. From top to bottom: total (luminous + dark) three dimensional mass density ρ, dark matter density $\rho_{\rm DM,dyn}$ and luminous mass density $\rho_{*,\rm dyn}$. All densities are spherically averaged. Left-hand panels: galaxies with less massive halos ($v_h \leqslant 400\,$km/s); right-hand panels: galaxies with massive halos ($v_h > 400\,$km/s. In the middle row the dotted lines indicate the spatial region where $\rho_{\rm DM,dyn} < \rho_{*,\rm dyn}/10$.

5 DARK MATTER

5.1 Mass that does not follow the light

Fig. 13 shows the spherically averaged three dimensional density distributions of luminous and dark matter, as well as the sum of both. The sample is subdivided into galaxies with LOG-halo circular velocities $v_h \leqslant 400\,$km/s and galaxies with $v_h > 400\,$km/s. The reason is that the latter galaxies

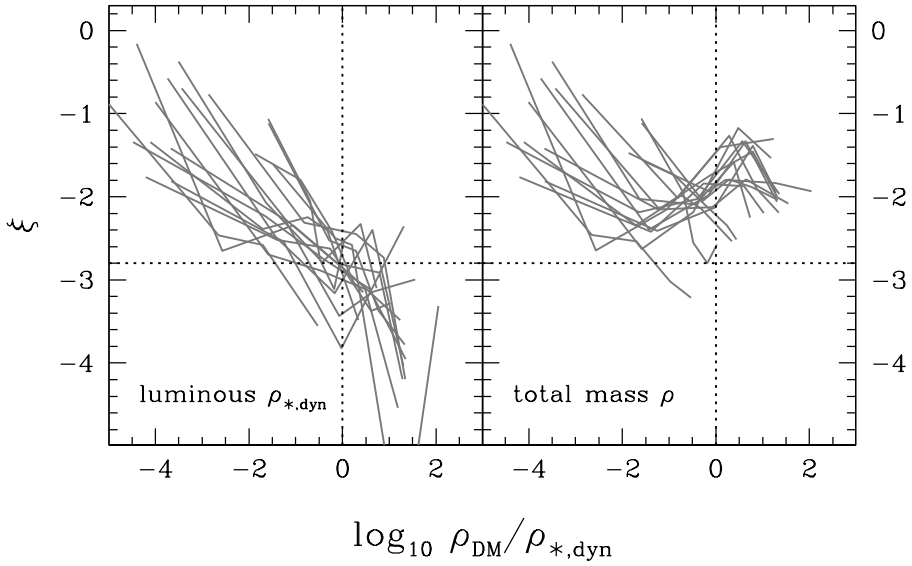

Figure 14. Comparison of the local logarithmic density slope $\xi = \mathrm{d}\ln\rho(r)/\mathrm{d}\ln(r)$ with the density ratio $\rho_{\rm DM}(r)/\rho_{*,\rm dyn}(r)$ of dark to luminous matter at the same radius. Left panel: logarithmic slope of the luminous mass density $\rho_{*,\rm dyn} = \Upsilon_{*,\rm dyn} \times \nu$; right panel: logarithmic slope of the total mass density $\rho = \Upsilon_{*,\rm dyn} \times \nu + \rho_{\rm DM}$. Vertical dotted lines indicate where luminous and dark matter equalise. To the left of these lines luminous mass dominates (inner regions of the galaxies), to the right dark matter dominates (outer regions of galaxies). Horizontal lines are for $\xi = -2.8$, the luminous slope at which dark matter takes over luminous matter.

have very uniform outer dark and total mass density profiles. The corresponding dark matter fractions (inside $r_{\rm eff}$) scatter around a mean of $\langle f_{\rm DM,dyn}\rangle = 23 \pm 17\,\%$ and do not depend on $\sigma_{\rm eff}$. Note that in the central galaxy regions our models implicitly maximise the mass contribution from the light. Similar maximum-bulge models for lensing galaxies yield dark matter fractions around 25 % as well (Barnabè et al. 2009).

Fig. 14 shows the logarithmic slope of the luminosity density and the total mass density in the Coma galaxies. The slope is plotted against the ratio of dark to luminous matter densities at the same radii. In the inner regions the slope of the total mass density follows the light, since dark matter is negligible ($\rho_{*,\rm dyn} \gg \rho_{\rm DM}$), in the outer regions the total mass density profile is flatter than the light profile. Overall, the total mass density is roughly isothermal: $\rho \sim r^{-2}$. This reflects the nearly flat circular velocity curves of early-type galaxies (Gerhard et al. 2001; Thomas et al. 2007b). Similar slopes for the total mass distribution have been seen in lensing galaxies (Koopmans et al. 2006; Barnabe et al. 2011). Fig. 14 illustrates that the actual need for a dark matter component in our models comes from the fact that the outer mass distribution does not follow the light in early-type galaxies. The radius where the density of dark matter takes over luminous matter is roughly where the slope of the luminosity density falls below $\xi \approx -2.8$ (indicated by the horizontal dotted lines in Fig. 14).

5.2 A component of dark matter that follows the light?

A galaxy might have more dark matter than captured by $\rho_{\rm DM}$ if some fraction of the halo mass follows the light so closely that it is mapped onto $\Upsilon_{*,\rm dyn}$ rather than $\rho_{\rm DM}$. In particular, Fig. 14 leaves the possibility open that this could happen in the inner galaxy regions where the slope of the luminosity distribution is $-2 \lesssim \xi \lesssim -1$. If the fraction of dark matter that follows the light is larger in galaxies with higher $\sigma_{\rm eff}$, then this would be a possible explanation for the trend between $\Upsilon_{*,\rm dyn}/\Upsilon_{\rm Krou}$ and $\sigma_{\rm eff}$ seen in Fig. 10.

Because the *total* (luminous + dark) mass $M_{\rm tot,dyn}$ is well constrained by the dynamical models (inside the region with kinematical data), a spurious increase in the luminous mass component would be accompanied by a corresponding decrease in the nominal dark matter fraction $f_{\rm DM,dyn}$ of the models. More specifically, under the assumption $M_{\rm tot,dyn} = M_{\rm tot,gal}$, the model parameters ($\Upsilon_{*,\rm dyn}, f_{\rm DM,dyn}$) and the actual galaxy parameters ($\Upsilon_{*,\rm gal}, f_{\rm DM,gal}$) would be related via

$$\Upsilon_{*,\rm dyn} = \Upsilon_{*,\rm gal} + (f_{\rm DM,gal} - f_{\rm DM,dyn})\ \Upsilon_{\rm tot,dyn}, \tag{7}$$

where $\Upsilon_{\rm tot,dyn} \equiv M_{\rm tot,dyn}/L$ is the total mass-to-light ratio (including dark matter). A degeneracy in the mass decomposition (at fixed *total* mass) would therefore correlate the offset

$$\Delta\Upsilon \equiv \frac{\Upsilon_{*,\rm dyn} - \Upsilon_{*,\rm gal}}{\Upsilon_{\rm Krou}} \tag{8}$$

in stellar mass-to-light ratios with the offset

$$\Delta f_{\rm DM} \equiv f_{\rm DM,dyn} - f_{\rm DM,gal} \tag{9}$$

in dark matter fractions as

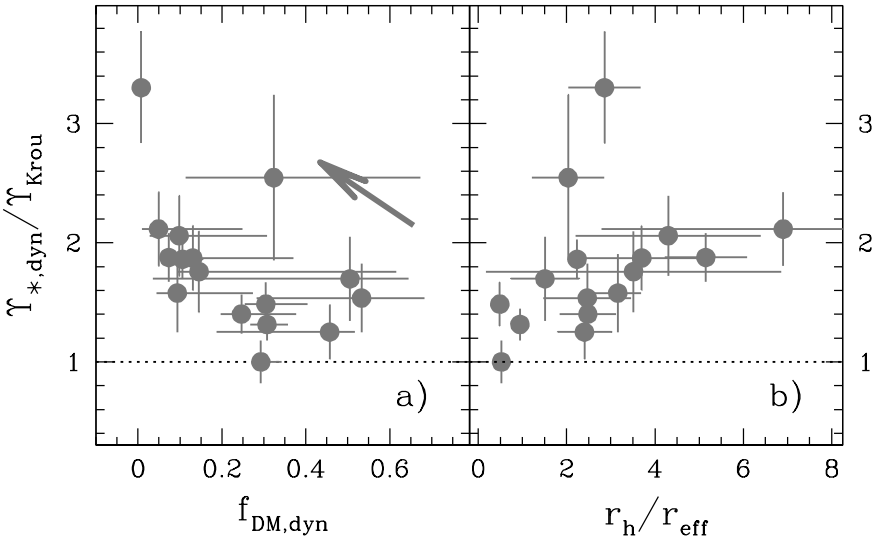

Figure 15. $\Upsilon_{*,\rm dyn}/\Upsilon_{\rm Krou}$ against dark matter fraction $f_{\rm DM,dyn}$ (panel a) and against halo core radius r_h (scaled by the effective radius $r_{\rm eff}$; panel b). Shifting mass from the dark halo component into the luminous one at constant *total* mass moves galaxies along the direction indicated by the arrow in the left-hand panel (a). Note that for the right-hand panel the galaxy GMP1990 has been omitted, since its dark matter fraction is so low that the determination of a halo core-radius becomes meaningless.

$$\Delta\Upsilon = -\frac{\Upsilon_{\rm tot,dyn}}{\Upsilon_{\rm Krou}}\Delta f_{\rm DM}. \quad (10)$$

Fig. 15a shows $\Upsilon_{*,\rm dyn}/\Upsilon_{\rm Krou}$ against the models' dark matter fractions $f_{\rm DM,dyn}$ (inside $r_{\rm eff}$). There is a slight trend for $\Upsilon_{*,\rm dyn}/\Upsilon_{\rm Krou}$ to be particularly large whenever $f_{\rm DM,dyn}$ is low. Note that an intrinsic dark matter variation from galaxy to galaxy at a constant IMF scatters galaxies horizontally in Fig. 15a, while an IMF variation at constant dark matter fraction scatters galaxies vertically. The luminous-dark matter degeneracy discussed above scatters galaxies along the arrow shown in Fig. 15a. It marks the direction along which the fitted $(\Upsilon_{*,\rm dyn}, f_{\rm DM,dyn})$ are expected to separate from the galaxies' $(\Upsilon_{*,\rm gal}, f_{\rm DM,gal})$ according to equation (10) and – for each galaxy – depends on the ratio $\Upsilon_{\rm tot,dyn}/\Upsilon_{\rm Krou}$. For the arrow in Fig. 15a we have used the average $\langle\Upsilon_{\rm tot,dyn}/\Upsilon_{\rm Krou}\rangle = 2.39$ over the Coma sample. The distribution of the majority of Coma galaxies roughly follows the arrow, in particular below $f_{\rm DM,dyn} \lesssim 0.3$.

Fig. 15a suggests, though does not unambiguously prove, that the scatter in $\Upsilon_{*,\rm dyn}/\Upsilon_{\rm Krou}$ could reflect a degeneracy in the dynamical mass decomposition. A contamination of some $\Upsilon_{*,\rm dyn}$ with dark matter would also explain the trend seen in Fig. 15b, where $\Upsilon_{*,\rm dyn}/\Upsilon_{\rm Krou}$ is plotted against the halo core-radius r_h (in units of $r_{\rm eff}$). The more the inner dark matter goes into $\Upsilon_{*,\rm dyn}$, the less the model component $\rho_{\rm DM}$ traces the actual inner dark matter of the galaxies. Instead, it only represents the outer parts of the dark matter halos. Correspondingly, one would expect relatively larger halo core-radii (with respect to $r_{\rm eff}$) whenever $\Upsilon_{*,\rm dyn}$ is large compared to $\Upsilon_{\rm ssp}$ – as seen in Fig. 15b.

Napolitano et al. (2010) analysed a large set of early-type galaxies with two-component spherical Jeans models and find dynamical $\Upsilon_{*,\rm dyn}$ close to the Salpeter IMF when using collisionless halos from cosmological simulations without baryon contraction. However, their $\Upsilon_{*,\rm dyn}$ get closer to the Kroupa IMF when baryonic contraction is taken into account. Baryonic contraction might therefore be one way to make luminous and dark matter distributions similar enough to explain the difference between $\Upsilon_{*,\rm dyn}$ and $\Upsilon_{\rm Krou}$ (see Sec. 5.4).

In our modelling approach, the halo parameters are allowed to vary freely, without being connected to results from cosmological simulations. On the one hand this ensures that baryonic contraction is implicitly taken into account: the best-fit models for more contracted halos are simply expected to occur in a different region of parameter space. On the other hand, the steepest halo density profiles that we probed are those from cosmological simulations without baryon contraction (NFW halos; cf. Sec. 2.1). If the actual galaxy halo profiles are steeper, then the best-fit dynamical model would still be obtained by shifting some fraction of the inner dark mass into $\Upsilon_{*,\rm dyn}$.

More similar distributions of luminous and dark matter in some galaxies than in others could also reflect differences in their evolutionary histories. For example, the cosmological simulations of Naab, Johansson, & Ostriker (2009) indicate a difference in the radial distribution of in-situ formed stars relative to stars that were accreted during mergers. In-situ formed stars have a more centrally concentrated radial distribution than stars that were accreted in collisionless mergers. The latter dominate the stellar mass density around $r_{\rm eff}$. In any case, more detailed investigations of numerical simulations are required to conclude about a possible degeneracy between luminous and dark matter in the inner regions of galaxies.

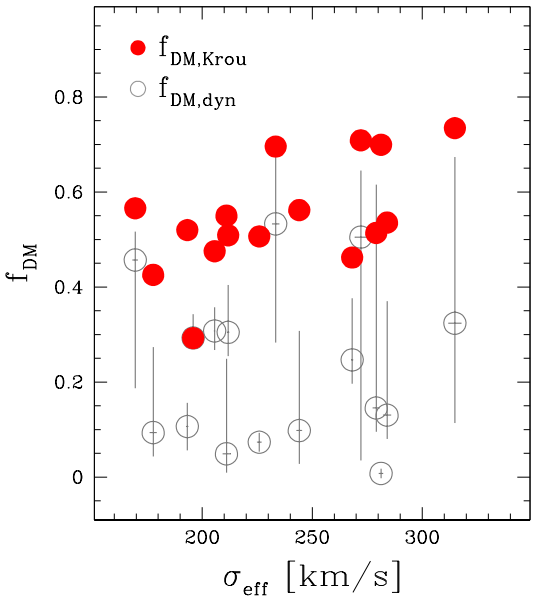

Figure 16. Dark matter fractions (inside the effective radius $r_{\rm eff}$) against velocity dispersion $\sigma_{\rm eff}$. Open circles: fraction of dark matter $f_{\rm DM,dyn}$ that does not follow the light; filled circles: dark matter fraction $f_{\rm DM,Krou}$ assuming i) a universal Kroupa IMF and ii) that the excess mass $(\Upsilon_{*,\rm dyn} - \Upsilon_{\rm Krou}) \times L$ is a component of dark matter that follows the light.

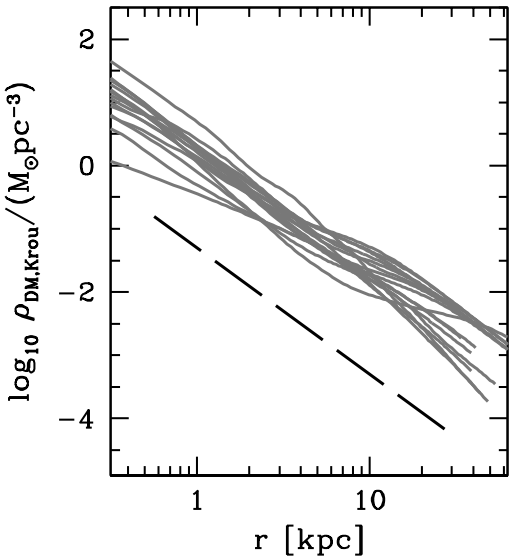

Figure 17. Spherically averaged dark matter density $\rho_{\rm DM,Krou}$ against radius. The excess mass $(\Upsilon_{*,\rm dyn} - \Upsilon_{\rm Krou}) \times L$ with respect to a Kroupa IMF stellar population has been added to the dark matter halo. The dashed line indicates a power-law density with logarithmic slope of -2.

5.3 The distribution of dark matter in case of a universal Kroupa IMF

If we adopt the point of view that the stellar IMF in early-type galaxies is universal and Kroupa-like then this affects the distribution of dark matter significantly. The reason is that in this case our nominal halo component captures only a part of the galaxies' dark matter, while a large fraction follows the light and is included in $\Upsilon_{*,\rm dyn}$. In fact, a universal Kroupa IMF implies the dark matter fractions $f_{\rm DM,Krou}$ to read

$$f_{\rm DM,Krou}(r) \equiv f_{\rm DM,dyn}(r) + \frac{(\Upsilon_{*,\rm dyn} - \Upsilon_{\rm Krou}) \times L(r)}{M_{\rm tot,dyn}(r)}. \quad (11)$$

These fractions are larger than the nominal $f_{\rm DM,dyn}$ derived from $\rho_{\rm DM}$, have a smaller scatter and slightly increase with galaxy $\sigma_{\rm eff}$ (cf. Fig. 16).

Fig. 17 shows the spherically averaged dark matter density profiles

$$\rho_{\rm DM,Krou} \equiv \rho_{\rm DM} + (\Upsilon_{*,\rm dyn} - \Upsilon_{\rm Krou}) \times \nu \quad (12)$$

including the extra dark matter required for a Kroupa IMF (cf. equation 2). These density profiles are smooth and close to a power-law with logarithmic slope slightly shallower than -2. The slight wiggles in the profiles around ≈ 5 kpc indicate the transition from the outer parts, which are dominated by $\rho_{\rm DM}$, to the inner parts, which are dominated by the second term on the right-hand side of equation (12).

5.4 Dark matter density and halo assembly epoch

In Thomas et al. (2009b) we estimated halo assembly epochs $z_{\rm form}$ based on the assumption that the average dark matter density $\langle\rho_{\rm DM}\rangle$ inside $2\,r_{\rm eff}$ scales with $(1+z_{\rm form})^3$. From the overdensity of dark matter in early-type relative to spiral galaxies one can then narrow down elliptical galaxy assembly redshifts with an additional assumption about the typical formation redshift of spiral galaxies ($z_{\rm form} \approx 1$). Adopting a universal Kroupa IMF results in average dark matter densities a factor of ≈ 3 larger than the nominal ones of the dynamical models. The strongest contribution to this increase comes from the single galaxy GMP1990 which has a negligible $f_{\rm DM,dyn}$, but a large $\Upsilon_{*,\rm dyn}/\Upsilon_{\rm Krou}$. Without this galaxy, dark matter densities are only larger by about a factor of 1.6, which lets the halo assembly redshifts increase from $z_{\rm form} \approx 1-3$ (Thomas et al. 2009b) to about $z_{\rm form} \approx 1.5-3.5$.

As a second test, we have compared the $\rho_{\rm DM,Krou}$ from Fig. 17 directly to the galaxy formation models of De Lucia & Blaizot (2007). These models do not include the dynamical reaction of dark matter on the baryon infall. Therefore, we first subtracted from the observed dark matter profile $\rho_{\rm DM,Krou}$ the expected effect of baryon contraction by assuming the adiabatic approximation (i.e. by inverting the equations of Blumenthal et al. 1986). The relationship between the average dark matter density and halo formation redshift in the models of De Lucia & Blaizot (2007) is well fitted by $\log\langle\rho_{\rm DM}\rangle \approx -2.9 + \log(1+z_{\rm form})^3$. We used this relation to calculate Coma galaxy assembly redshifts from the decontracted Kroupa dark matter halo densities. Fig. 18 shows that these halo assembly redshifts cover a similar range ($z_{\rm form} \approx 1-3$) as the ones obtained through the comparison with spiral galaxy dark matter densities. Note that we here computed star-formation redshifts from the average stellar ages inside $r_{\rm eff}$, while in Thomas et al. (2009b) we used the central stellar ages from Mehlert et al. (2003).

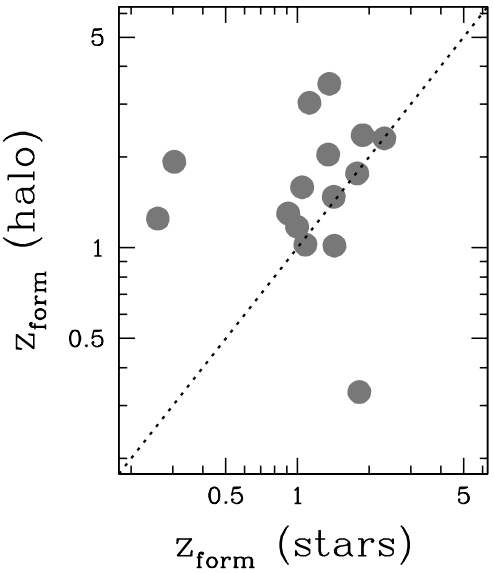

Figure 18. Star formation epoch (x-axis) against halo assembly epoch (y-axis). The dotted line represents the one-to-one relation.

For many of the Coma galaxies, star formation redshifts and dark halo assembly redshifts are similar. Two galaxies appear far to the left of the one-to-one relation. These are GMP0756 and GMP1176, which have extended and relatively young ($\tau \approx 3\,\mathrm{Gyr}$) stellar disks. The galaxy on the bottom-right, where the stars seem significantly older than the halo is GMP5568. As discussed in Thomas et al. (2009b), dry mergers can move galaxies below the one-to-one relation in Fig. 18. Besides this possibility the effective radius of GMP5568 is exceptionally large ($r_{\rm eff} \approx 27\,\mathrm{kpc}$). Therefore, the dark matter density refers to a spatial region significantly larger than in any of our other Coma galaxies. If the effective radius of this galaxy was overestimated, then the average dark matter density would be underestimated and so would be the halo assembly redshift. This could also explain the high dark matter fraction of GMP5568 (cf. Tab. 1), since it generally increases with the physical distance from the galaxy centre.

6 THE TILT OF THE FUNDAMENTAL PLANE

The effective radius $r_{\rm eff}$, mean surface brightness $\langle I\rangle_{\rm eff}$ inside $r_{\rm eff}$ and the central velocity dispersion σ_0 of a galaxy are connected via

$$\sigma_0^2 = c_M \frac{G\,M}{r_{\rm eff}} \tag{13}$$

where M is the total mass and

$$\langle I\rangle_{\rm eff} = \frac{L}{2\pi\, r_{\rm eff}^2} \tag{14}$$

where L is the total luminosity. In virial equilibrium the structure coefficient c_M depends on the orbital structure and the radial distributions of the mass and the tracer population. For a homologous family of dynamical objects c_M is a constant and with $\langle\Upsilon\rangle \equiv M/L$ equations (13) and (14) lead to

$$\log\frac{r_{\rm eff}}{\rm kpc} = 2\,\log\frac{\sigma_0}{\rm km/s} - \log\frac{\langle I\rangle_{\rm eff}}{\rm L_\odot pc^{-2}} + \gamma \tag{15}$$

and

$$\gamma = -\log\frac{\langle\Upsilon\rangle}{\rm M_\odot/L_{\mathit{R},\odot}} - \log\left(2\pi\,\frac{G}{(\rm km/s)^2\,kpc\,M_\odot^{-1}} c_M\right). \tag{16}$$

The actually observed fundamental plane (FP; Djorgovski & Davis 1987; Dressler et al. 1987) of early-type galaxies reads

$$\log\frac{r_{\rm eff}}{\rm kpc} = \alpha\,\log\frac{\sigma_0}{\rm km/s} + \beta\,\log\frac{\langle I\rangle_{\rm eff}}{\rm L_\odot pc^{-2}} + \gamma \tag{17}$$

with $\alpha \neq 2$ and $\beta \neq -1$. It is tilted with respect to the virial plane of equation (15).

Fig. 19a shows the FP[2] of Coma galaxies. The best-fit parameters of an orthogonal fit are $\alpha = 1.26 \pm 0.58$ and $\beta = -0.72 \pm 0.10$ (bootstrap errors). Within the statistical uncertainties, the fit is consistent with the r-band FP of SDSS early-type galaxies ($\alpha = 1.49 \pm 0.05$, $\beta = -0.75 \pm 0.01$; Bernardi et al. 2003; Hyde & Bernardi 2009). The larger errors result from the smaller sample size. Most of the difference with respect to Bernardi et al. (2003) goes back to four galaxies (GMP0144, GMP0756, GMP1176, and GMP5975) that are distinct from the rest of the sample in several respects: (1) they have young central stellar cores ($\tau_0 < 7\,\mathrm{Gyr}$; cf. Mehlert et al. 2003); (2) at least two of them have an extended thin stellar disk; (3) they follow different dark halo scaling relations (Thomas et al. 2009b). Fig. 20 is equivalent to Fig. 19 except that these four galaxies have been removed. The corresponding FP matches well with the SDSS results.

6.1 The fundamental mass plane

The tilt in the FP can reflect non-homology (i.e. c_M being a function of galaxy mass) or variations in $\langle\Upsilon\rangle$ (or both). A systematic variation of $\langle\Upsilon\rangle$, in turn, could reflect stellar population effects or changes in the dark matter distribution. In any case, the dynamical models allow to incorporate variations of $\langle\Upsilon\rangle$ into the FP. For this purpose let $\langle\Sigma\rangle_{\rm eff}$ denote the average surface mass density inside $r_{\rm eff}$. Then, equation (17) can be written

$$\log\frac{r_{\rm eff}}{\rm kpc} = \alpha\,\log\frac{\sigma_0}{\rm km/s} + \beta\,\log\frac{\langle\Sigma\rangle_{\rm eff}}{\rm M_\odot pc^{-2}} + \gamma, \tag{18}$$

where

$$\gamma = -\log\left(2\pi\,\frac{G}{(\rm km/s)^2\,kpc\,M_\odot^{-1}} c_M\right). \tag{19}$$

Equation (18) defines the so-called fundamental mass plane (Bolton et al. 2007).

Figs. 19b - 19d show Coma galaxy MPs for different choices of $\langle\Sigma\rangle_{\rm eff}$. Using either $\langle\Sigma\rangle_{\rm Krou} \equiv \Upsilon_{\rm Krou} \times \langle I\rangle_{\rm eff}$ (panel b) or $\langle\Sigma\rangle_{*,\rm dyn} \equiv \Upsilon_{*,\rm dyn} \times \langle I\rangle_{\rm eff}$ (panel c), the tilt is reduced, but does not vanish ($\beta \neq -1$). The change in α

[2] Note that in this section we use the average velocity dispersion σ_0 inside the central $2''$, derived in the same way as the effective $\sigma_{\rm eff}$ discussed in Sec. 3.

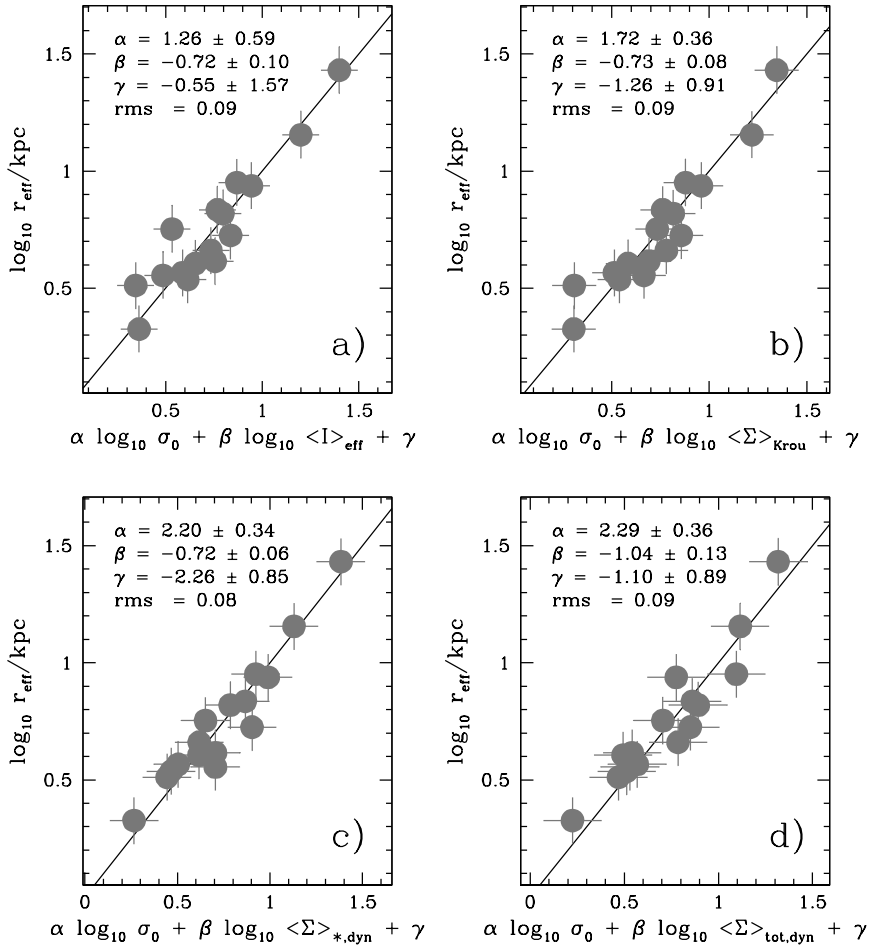

Figure 19. Fundamental plane and mass plane of 16 Coma galaxies. In each panel the best-fit parameters of an orthogonal fit and the rms-scatter in log $r_{\rm eff}$ are quoted. a) Traditional FP; b) fundamental mass plane from stellar populations, i.e. the effective surface brightness is $\langle I\rangle_{\rm eff}$ is replaced by the mass-density $\langle\Sigma\rangle_{\rm eff} \equiv \Upsilon_{\rm Krou} \times \langle I\rangle_{\rm eff}$; c) as b) but for the dynamically derived stellar-population $\Upsilon_{*,\rm dyn}$: $\langle\Sigma\rangle_{*,\rm dyn} \equiv \Upsilon_{*,\rm dyn} \times \langle I\rangle_{\rm eff}$; d) as c), but instead of the dynamically derived *stellar* mass-to-light ratio the *total* $M_{\rm tot,dyn}/L$ (including dark matter) is used: $\langle\Sigma\rangle_{\rm tot,dyn} \equiv M_{\rm tot,dyn}/L \times \langle I\rangle_{\rm eff}$ ($M_{\rm tot,dyn}/L$ is taken at the effective radius). Solid lines trace the one-to-one relation.

from Fig. 19a to Fig. 19b is consistent with the SDSS analysis of Hyde & Bernardi (2009). Fig. 19d shows the case of $\langle\Sigma\rangle_{\rm eff}$ including all the projected mass (luminous and dark) inside $r_{\rm eff}$, respectively. The mass plane of Fig. 19d is tilt-free within the errors. The match to the virial plane of equation (15) improves further when omitting the four galaxies harbouring young stellar cores (cf. Fig. 20). With $\langle\Upsilon\rangle \equiv M_{\rm tot,dyn}/L$ the MP has the same scatter as the FP itself (cf. Figs. 19a and d). For the subsample of old Coma galaxies the scatter slightly increases (cf. Fig. 20).

6.2 The tilt of the fundamental plane

The tilt in the FP is reduced when the effective surface brightness is replaced by an effective surface mass derived from $\Upsilon_{\rm ssp}$[3]. The amount of reduction is consistent with the SDSS results of Hyde & Bernardi (2009). In accordance with Graves & Faber (2010), the tilt is further reduced if $\Upsilon_{\rm ssp}$ is replaced by the dynamical $\Upsilon_{*,\rm dyn}$. As discussed above, the different scalings of $\Upsilon_{*,\rm dyn}$ and $\Upsilon_{\rm ssp}$ with $\sigma_{\rm eff}$ could reflect (1) changes in the IMF or (2) changes in the distribution of dark matter. The absence of any correlation between $\Upsilon_{*,\rm dyn}/\Upsilon_{\rm Krou}$ and stellar population parameters makes (2) more likely than (1). Finally, the tilt vanishes completely (for a subsample of Coma galaxies with uniformly old stellar populations), if the remaining dark mass inside the effective

[3] In Sec. 6 the surface mass was derived from the Kroupa IMF, but the difference between the Kroupa and the Salpeter IMF is only a constant scaling factor. The results for the Salpeter IMF are therefore similar.

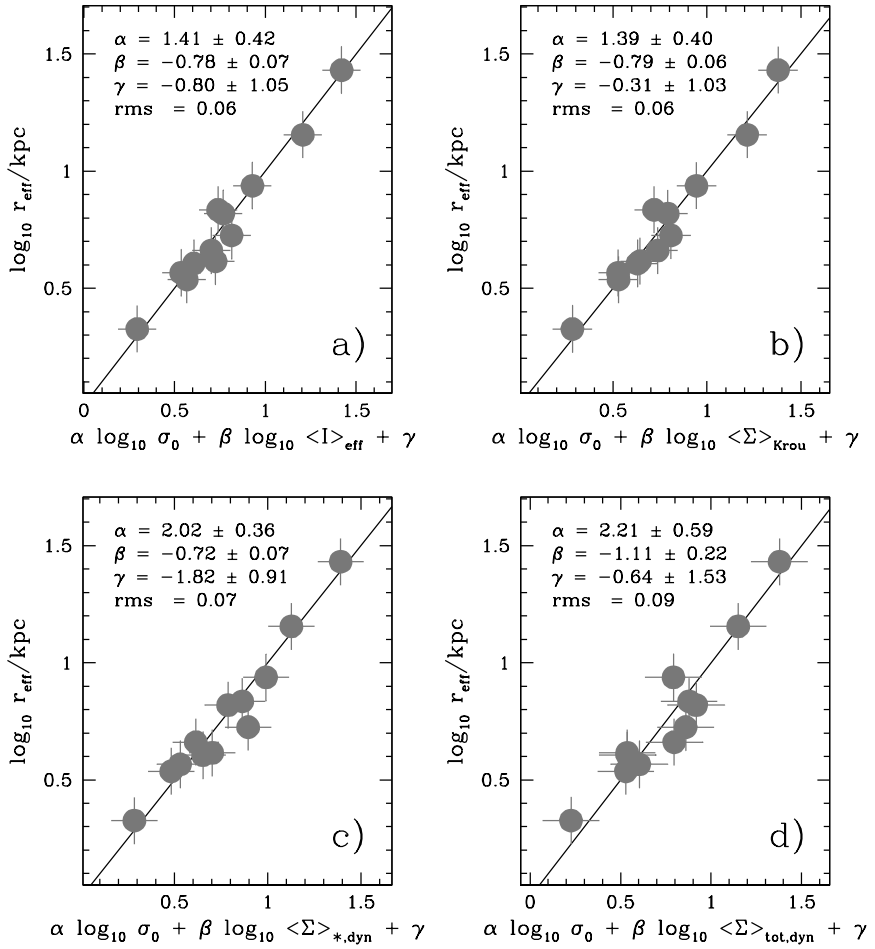

Figure 20. As Fig. 19, but four galaxies with young stellar cores are omitted.

radius $r_{\rm eff}$ is taken into account as well. This behaviour is also found in lensing studies (Bolton et al. 2007).

In our FP analysis we have not tried to calculate c_M directly from the dynamical models. However, the density distribution (in particular the galaxy flattening) as well as the orbital structure vary among the Coma galaxies (Thomas et al. 2009a). Nevertheless, Fig. 20d indicates that for old Coma early-types the tilt of the FP is dominated by mass-to-light ratio effects rather than any possible variation in c_M.

6.3 Mass estimators

Wolf et al. (2010) provide an estimation for the mass

$$M_{\rm W10}(r_3) = \frac{3\langle\sigma^2\rangle r_3}{G} \qquad (20)$$

inside the radius r_3 where the logarithmic density slope of the tracer population is $\xi = -3$. Here, $\langle\sigma^2\rangle$ is the average of the projected σ^2 over the whole galaxy. Wolf et al. (2010) derived eq. (20) for non-rotating spherical galaxies. For the Coma galaxies, we averaged the measured σ^2 up to $r_{\rm eff}$, ignoring the galaxies' rotation velocities. Fig. 21a compares Coma galaxy masses $M_{\rm tot,dyn}(r_3)$ against the predictions of eq. (20). Averaged over all Coma galaxies we find $\langle M_{\rm tot,dyn}(r_3)/M_{\rm W10}(r_3)\rangle = 1.03 \pm 0.27$ (rms scatter). Fig. 21b is similar to Fig. 21a, except for the additional approximation $r_3 \approx r_{1/2} \approx 4/3\, r_{\rm eff}$, where $r_{1/2}$ is the deprojected half-light radius. The agreement with the Coma galaxies is still very good.

Fig. 22 compares luminous dynamical masses with the estimator

$$M_{\rm C06} = \frac{5\sigma^2_{\rm eff} r_{\rm eff}}{G}. \qquad (21)$$

from Cappellari et al. (2006). When using luminous dynamical masses $M_{*,\rm dyn} = \Upsilon_{*,\rm dyn} \times L$ from model fits that do have a separate dark matter component, then we find $\langle M_{*,\rm dyn}/M_{\rm C06}\rangle = 0.86 \pm 0.35$ (cf. Fig. 22a). The small offset disappears if we use model fits that do not have an additional dark matter component (equivalent to the approximation made in Cappellari et al. 2006). The corresponding

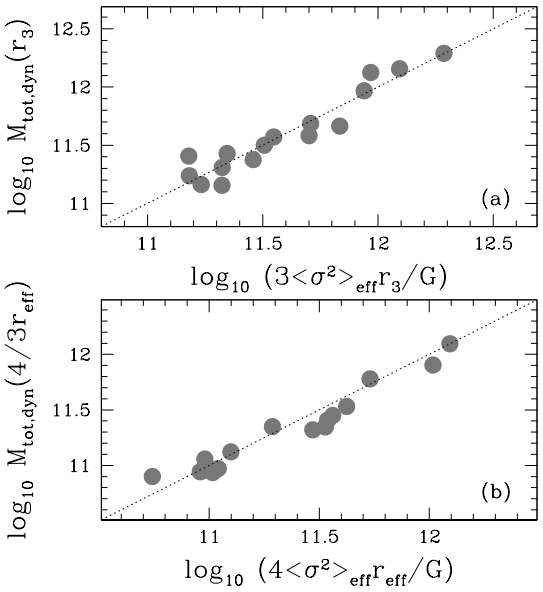

Figure 21. Comparison of Coma galaxies with the Wolf et al. (2010) mass estimator (cf. eq. 20): (a) total dynamical mass enclosed inside the radius r_3, where the logarithmic slope of the luminosity distribution equals $\xi = -3$; (b) is similar to (a) but with the additional approximation $r_3 \approx 4/3\, r_{\rm eff}$.

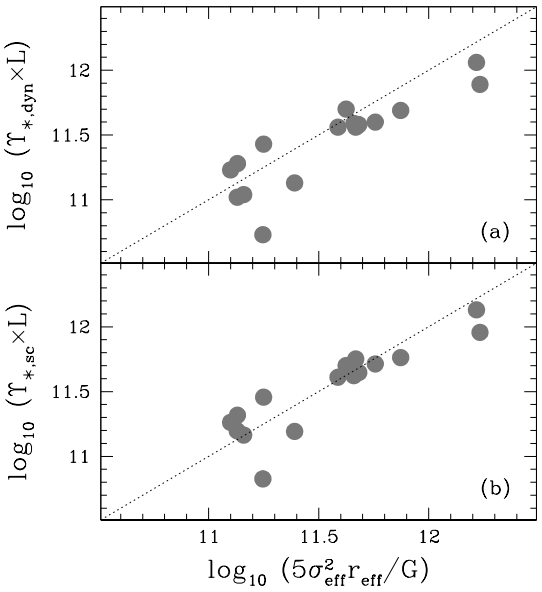

Figure 22. Comparison of Coma galaxies with the Cappellari et al. (2006) virial mass estimator (cf. eq. 21): (a) luminous dynamical mass $\Upsilon_{*,\rm dyn} \times L$ from fits explicitly allowing for a separate component of dark matter; (b) luminous dynamical mass $\Upsilon_{*,sc} \times L$ from fits assuming that all the mass follows the light.

luminous dynamical masses $M_{*,\rm sc} = \Upsilon_{*,\rm sc} \times L$ (cf. Tab. 1) are slightly larger and the comparison with eq. (21) yields $\langle M_{*,\rm sc}/M_{\rm C06}\rangle = 1.01 \pm 0.36$ (cf. Fig. 22). The rms scatter includes both the measurement errors and anisotropy variations (Thomas et al. 2007b). Note, however, that the assumption that all the mass follows the light is inconsistent with lensing masses (cf. Fig. 5).

Thus, the Wolf et al. (2010) formula gives good estimates for the *total* dynamical mass inside a radius which is a bit larger than $r_{\rm eff}$. The virial estimator of Cappellari et al. (2006) captures the entire dynamical mass that results under the assumption that *total mass follows light*. Assuming $r_3 \approx r_{1/2}$, eq. (21) implies

$$M_{\rm C06}(r_3) \approx M_{\rm C06}(r_{1/2}) = \frac{M_{\rm C06}}{2} = \frac{2.5\sigma^2_{\rm eff} r_{\rm eff}}{G}, \qquad (22)$$

whereas from eq. 20 and $r_3 \approx 4/3\, r_{\rm eff}$ it follows

$$M_{\rm W10}(r_3) \approx \frac{4\langle\sigma^2\rangle r_{\rm eff}}{G}. \qquad (23)$$

Concerning the enclosed mass inside $4/3 r_{\rm eff}$, the two mass estimators would differ by a factor $4/2.5 = 1.6$, unless $\langle\sigma^2\rangle \neq \sigma^2_{\rm eff}$. Due to the different treatment of rotation $\sigma^2_{\rm eff} \approx 1.3\,\langle\sigma^2\rangle$ in the Coma sample, such that the actual difference is only about 20 percent.

7 SUMMARY

We compared dynamically derived stellar mass-to-light ratios $\Upsilon_{*,\rm dyn}$ with completely independent results from simple stellar population models. Our dynamical models are based on Schwarzschild's orbit superposition technique and have two mass components. One follows the light and its mass-to-light ratio $\Upsilon_{*,\rm dyn}$ is assumed to approximate the stellar mass distribution. The other mass component explicitly accounts for dark matter. This way, any potential degeneracy between the stellar mass and the dark matter halo is minimised. The Coma galaxy sample studied here is currently the largest with axisymmetric Schwarzschild models including dark matter explicitly.

Intrinsic uncertainties in the modelling, in particular related to the assumption of axial symmetry, are unlikely to bias our results significantly. The main reason is that in projection, our dynamical masses match well with completely independent results from strong gravitational lensing.

Our main findings are:

(i) For galaxies with low velocity dispersions ($\sigma_{\rm eff} \approx 200\,$km/s), the assumption that all the mass follows the light yields projected masses larger than in comparable strong-gravitational lens systems.

(ii) In high-velocity dispersion galaxies ($\sigma_{\rm eff} \approx 300\,$km/s) the assumption that mass follows light is consistent with strong lensing results.

(iii) Two-component dynamical models with an explicit dark halo component yield total projected masses that are in good agreement with results from strong gravitational lensing for all galaxies.

(iv) In two-component models, the mass-to-light ratio $\Upsilon_{*,\rm dyn}$ of the component that follows the light increases with galaxy velocity dispersion $\sigma_{\rm eff}$.

(v) Stellar population $\Upsilon_{\rm ssp}$ (for any fixed IMF) are largely independent of $\sigma_{\rm eff}$. As a result, the ratio $\Upsilon_{*,\rm dyn}/\Upsilon_{\rm ssp}$ of luminous dynamical mass over stellar population mass increases with galaxy velocity dispersion.

(vi) The luminous dynamical $\Upsilon_{*,\rm dyn}$ is always larger than, or at least equalises, the stellar-population mass-to-light ratio $\Upsilon_{\rm Krou}$ for a Kroupa IMF.

(vii) There is no correlation between $\Upsilon_{*,\rm dyn}/\Upsilon_{\rm ssp}$ and stellar population age, metallicity or [α/Fe] ratio.

(viii) Inside $r_{\rm eff}$, the average fraction of dark matter (that does not follow the light) is $f_{\rm DM,dyn} = 28\pm17\,\%$ in the Coma galaxies.

(ix) The tilt of the FP reduces if the effective surface brightness $\langle I\rangle_{\rm eff}$ is replaced by the stellar population surface-mass density $\Upsilon_{\rm ssp}\times\langle I\rangle_{\rm eff}$, further reduced if $\langle I\rangle_{\rm eff}$ is replaced by the dynamical stellar surface-mass density $\Upsilon_{*,\rm dyn}\times\langle I\rangle_{\rm eff}$ and, for a subsample of galaxies with uniformly old stellar populations, vanishes completely with the *total* dynamical surface-mass density $\langle\Sigma_{\rm tot,dyn}\rangle_{\rm eff}$.

(x) Commonly used mass estimators are accurate to the $20-30\,\%$ level.

The implications of these findings are as follows:

(i) That luminous dynamical masses increase more rapidly with galaxy velocity dispersion than stellar-population masses for a fixed IMF could be due to a change in the IMF or due to an increasing amount of dark matter following a spatial distribution similar to that of the light.

(ii) If the IMF changes, then massive early-types ($\sigma_{\rm eff}\approx 300\,$km/s) have up to two times more stellar mass per stellar light than lower-mass galaxies ($\sigma_{\rm eff}\approx 200\,$km/s), which are consistent with a Kroupa IMF. However, the lack of any correlation between $\Upsilon_{*,\rm dyn}/\Upsilon_{\rm ssp}$ and stellar population age, metallicity or [α/Fe] ratio is consistent with, though does not prove, that the IMF is actually universal.

(iii) If the IMF is universal, then the increase in luminous dynamical masses must primarily come from a component of dark matter that follows the light very closely and is more important in more massive galaxies. The IMF would be consistent with being Kroupa in all early-types.

(iv) Independent of the actual slope of the stellar IMF, luminous dynamical masses are *on average* more accurately predicted by assuming a Salpeter IMF: $\langle\Upsilon_{*,\rm dyn}/\Upsilon_{\rm Salp}\rangle = 1.15$, but these masses may not represent exclusively stars. The Kroupa IMF yields $\langle\Upsilon_{*,\rm dyn}/\Upsilon_{\rm Krou}\rangle = 1.8$.

(v) Adopting a Kroupa IMF and counting the excess mass $(\Upsilon_{*,\rm dyn}-\Upsilon_{\rm Krou})\times L$ as dark matter that follows the light doubles the average dark matter fractions inside $r_{\rm eff}$ to about $f_{\rm DM,Krou}\approx 55\pm12\,\%$. Moreover, it yields a smooth trend between the resulting $f_{\rm DM,Krou}$ and galaxy velocity dispersion and, also, smooth dark matter halo profiles.

(vi) The FP tilt is not a pure stellar population effect. Further inferences about the tilt depend on the interpretation of the observed $\Upsilon_{*,\rm dyn}/\Upsilon_{\rm Krou}$. As above, that the tilt reduces when considering the dynamical mass $\Upsilon_{*,\rm dyn}\times L$ that follows the light could be due to (1) variations in the relative distribution of luminous and dark matter or (2) IMF variability.

ACKNOWLEDGEMENTS

We thank the referee Glenn van de Ven for useful comments that helped us to improve the presentation of the results. JT acknowledges financial support by the DFG through SFB 375 "Astro-Teilchenphysik". RPS acknowledges support by the DFG Cluster of Excellence "Origin and Structure of the Universe". EMC is supported by the University of Padua through grants 60A02-1283/10 and CPDA089220 and by the Ministry of Education, University, and Research (MIUR) through grant EARA 2004-2006. SS acknowledges support by the TR33 "The Dark Universe" and by the Cluster of Excellence "Origin and Structure of the Universe". The new Coma galaxy HST observations were obtained through the program HSTGO-10884.0-A which was provided by NASA through a grant from the Space Telescope Science Institute, which is operated by the Association of Universities for Research in Astronomy, Inc. under NASA contract NAS5-26555. Funding for the SDSS and SDSS-II has been provided by the Alfred P. Sloan Foundation, the Participating Institutions, the National Science Foundation, the U.S. Department of Energy, the National Aeronautics and Space Administration, the Japanese Monbukagakusho, the Max Planck Society and the Higher Education Funding Council for England. The SDSS Web Site is http://www.sdss.org/. The SDSS is managed by the Astrophysical Research Consortium for the Participating Institutions. The Participating Institutions are the American Museum of Natural History, Astrophysical Institute Potsdam, University of Basel, University of Cambridge, Case Western Reserve University, University of Chicago, Drexel University, Fermilab, the Institute for Advanced Study, the Japan Participation Group, Johns Hopkins University, the Joint Institute for Nuclear Astrophysics, the Kavli Institute for Particle Astrophysics and Cosmology, the Korean Scientist Group, the Chinese Academy of Sciences (LAMOST), Los Alamos National Laboratory, the Max-Planck-Institute for Astronomy (MPIA), the Max-Planck-Institute for Astrophysics (MPA), New Mexico State University, Ohio State University, University of Pittsburgh, University of Portsmouth, Princeton University, the United States Naval Observatory and the University of Washington.

REFERENCES

Auger M. W., Treu T., Bolton A. S., Gavazzi R., Koopmans L. V. E., Marshall P. J., Bundy K., Moustakas L. A., 2009, ApJ, 705, 1099
Barnabè M., Czoske O., Koopmans L. V. E., Treu T., Bolton A. S., Gavazzi R., 2009, MNRAS, 399, 21
Barnabe M., Czoske O., Koopmans L. V. E., Treu T., Bolton A. S., 2011, arXiv, arXiv:1102.2261
Bender R., Burstein D., Faber S. M., 1992, ApJ, 399, 462
Bernardi M., et al., 2003, AJ, 125, 1866
Blumenthal G. R., Faber S. M., Flores R., Primack J. R., 1986, ApJ, 301, 27
Bolton A. S., Burles S., Treu T., Koopmans L. V. E., Moustakas L. A., 2007, ApJ, 665, L105
Cappellari M., et al., 2006, MNRAS, 366, 1126
Ciotti L., D'Ercole A., Pellegrini S., Renzini A., 1991, ApJ, 376, 380
Ciotti L., Lanzoni B., Renzini A., 1996, MNRAS, 282, 1
Corsini E. M., Wegner G., Saglia R. P., Thomas J., Bender R., Thomas D., 2008, ApJS, 175, 462
David L. P., Forman W., Jones C., 1991, ApJ, 369, 121
De Lucia G., Blaizot J., 2007, MNRAS, 375, 2
Djorgovski S., Davis M., 1987, ApJ, 313, 59

Dressler A., Lynden-Bell D., Burstein D., Davies R. L., Faber S. M., Terlevich R., Wegner G., 1987, ApJ, 313, 42
Ferreras I., Saha P., Leier D., Courbin F., Falco E. E., 2010, MNRAS, 409, L30
Gebhardt K., Richstone D., Tremaine S., Lauer T. R., Bender R., Bower G., Dressler A., Faber S. M., Filippenko A. V., Green R., Grillmair C., Ho L. C., Kormendy J., Magorrian J., Pinkney J., 2003, ApJ, 583, 92
Gerhard O., Kronawitter A., Saglia R. P., Bender R., 2001, AJ, 121, 1936
Godwin J. G., Metcalfe N., Peach J. V., 1983, MNRAS, 202, 113
Graves G. J., Faber S. M., 2010, ApJ, 717, 803
Grillo C., Gobat R., 2010, MNRAS, 402, L67
Hyde J. B., Bernardi M., 2009, MNRAS, 396, 1171
Kochanek C. S., 1991, ApJ, 373, 354
Koopmans L. V. E., Treu T., Bolton A. S., Burles S., Moustakas L. A., 2006, ApJ, 649, 599
Kroupa P., 2001, MNRAS, 322, 231
Maraston C., 1998, MNRAS, 300, 872
Maraston C., 2005, MNRAS, 362, 799
Maraston C., Strömbäck G., Thomas D., Wake D. A., Nichol R. C., 2009, MNRAS, 394, L107
Matsushita K., 2001, ApJ, 547, 693
Mehlert D., Saglia R. P., Bender R., Wegner G., 2000, A&AS, 141, 449
Mehlert D., Thomas D., Saglia R. P., Bender R., Wegner G., 2003, A&A, 407, 423
Naab T., Johansson P. H., Ostriker J. P., 2009, ApJ, 699, L178
Napolitano N. R., Romanowsky A. J., Tortora C., 2010, MNRAS, pp 793–+
Navarro J. F., Frenk C. S., White S. D. M., 1996, ApJ, 462, 563
Renzini A., Ciotti L., 1993, ApJ, 416, L49+
Richstone D. O., Tremaine S., 1988, ApJ, 327, 82
Saglia R. P., Bender R., Dressler A., 1993, A&A, 279, 75
Saglia R. P., et al., 2010, A&A, 509, A61
Salpeter E. E., 1955, ApJ, 121, 161
Scalo J. M., 1986, IAUS, 116, 451
Schwarzschild M., 1979, ApJ, 232, 236
Thomas D., Greggio L., Bender R., 1999, MNRAS, 302, 537
Thomas D., Maraston C., Bender R., 2003, MNRAS, 339, 897
Thomas D., Maraston C., Bender R., Mendes de Oliveira C., 2005b, ApJ, 621, 673
Thomas J., Saglia R. P., Bender R., Thomas D., Gebhardt K., Magorrian J., Richstone D., 2004, MNRAS, 353, 391
Thomas J., Saglia R. P., Bender R., Thomas D., Gebhardt K., Magorrian J., Corsini E. M., Wegner G., 2005a, MNRAS, 360, 1355
Thomas J., 2006, PhD thesis, LMU Munich
Thomas J., Jesseit R., Naab T., Saglia R. P., Burkert A., Bender R., 2007a, MNRAS, 381, 1672
Thomas J., Saglia R. P., Bender R., Thomas D., Gebhardt K., Magorrian J., Corsini E. M., Wegner G., 2007b, MNRAS, 382, 657
Thomas J., et al., 2009a, MNRAS, 393, 641
Thomas J., Saglia R. P., Bender R., Thomas D., Gebhardt K., Magorrian J., Corsini E. M., Wegner G., 2009b, ApJ, 691, 770
Treu T., Auger M. W., Koopmans L. V. E., Gavazzi R., Marshall P. J., Bolton A. S., 2010, ApJ, 709, 1195
Trujillo I., Burkert A., Bell E. F., 2004, ApJ, 600, L39
van de Ven G., Mandelbaum R., Keeton C. R., 2009, MNRAS, 398, 607
van Dokkum P., Conroy C., 2010, arXiv, arXiv:1009.5992
van Dokkum P., Conroy C., 2011, arXiv, arXiv:1102.3431
Wegner G., Corsini E. M., Saglia R. P., Bender R., Merkl D., Thomas D., Thomas J., Mehlert D., 2002, A&A, 395, 753
Wolf J., Martinez G. D., Bullock J. S., Kaplinghat M., Geha M., Muñoz R. R., Simon J. D., Avedo F. F., 2010, MNRAS, 406, 1220
York D. G., et al., 2000, AJ, 120, 1579

This paper has been typeset from a TEX/ LATEX file prepared by the author.